

# Valid time shifting Ensemble Kalman filter (VTS-EnKF) for dust storm forecasting

Mijie Pang<sup>1</sup>, Jianbing Jin<sup>1</sup>, Arjo Segers<sup>2</sup>, Huiya Jiang<sup>3</sup>, Wei Han<sup>4</sup>, Batjargal Buyantogtokh<sup>5</sup>, Ji Xia<sup>1</sup>, Li Fang<sup>1</sup>, Jiandong Li<sup>1</sup>, Hai Xiang Lin<sup>6,7</sup>, and Hong Liao<sup>1</sup>

<sup>1</sup>Joint International Research Laboratory of Climate and Environment Change, Jiangsu Key Laboratory of Atmospheric Environment Monitoring and Pollution Control, Jiangsu Collaborative Innovation Center of Atmospheric Environment and Equipment Technology, School of Environmental Science and Engineering, Nanjing University of Information Science and Technology, Nanjing, Jiangsu, China

<sup>2</sup>TNO, Department of Climate, Air and Sustainability, The Netherlands

<sup>3</sup>College of Environment and Resources, Nanjing Agricultural University

<sup>4</sup>Numerical Weather Prediction Center, Chinese Meteorological Administration, Beijing, China

<sup>5</sup>Information and Research Institute of Meteorology, Hydrology and Environment, Ulaanbaatar, Mongolia

<sup>6</sup>Delft Institute of Applied Mathematics, Delft University of Technology, Delft, The Netherlands

<sup>7</sup>Institute of Environment Sciences, Leiden University, The Netherlands

**Correspondence:** Jianbing Jin (jianbing.jin@nuist.edu.cn)

**Abstract.** Dust storms pose significant ~~threats to human risks to~~ health and property. ~~Accurate forecasting is crucial for taking precautionary measures. Dust models have suffered from uncertainties, necessitating accurate forecasting for preventive measures. Despite advancements, dust models grapple with uncertainties arising from emission and transport factors~~ processes. ~~Data assimilation can correct model bias by incorporating available observations, leading to improved analyses and forecasts~~ addresses ~~these by integrating observations to rectify model error, enhancing forecast precision.~~ The Ensemble Kalman Filter (EnKF) is a widely-used assimilation algorithm that effectively ~~tunes models~~ optimize model states, particularly in terms of intensity adjustment. However, ~~when the position of the simulation does not align consistently with the observations which is referred to as position error, the EnKF algorithm struggles. This is because when the position error is adequately large, EnKF can hardly represent this uncertainty. EnKF can be biased for the non-Gaussian statistics. In this paper, we proposed an~~ the ~~EnKF's efficacy is challenged by position errors between modeled and observed dust features, especially under substantial position errors. This study introduces the Valid Time Shifting-Ensemble Kalman Filter (VTS-EnKF~~ assimilation methodology, in which the standard EnKF is coupled) which combines stochastic EnKF with a valid time shifting method. In addition to the original ensembles quantifying dust loading variation, this methodology introduces extra ensembles from neighboring time for describing the potential spread of dust position. The enlarged ensemble captures both mechanism. By recruiting additional ensemble members from neighboring valid times, this method not only accommodates variations in dust load but also explicitly accounts for positional uncertainties. Consequently, the enlarged ensemble better represents both the intensity and positional errors, allowing observations to be thoroughly resolved into the assimilation calculations. We tested the thereby optimizing the utilization of observational data. The proposed VTS-EnKF on two super dust storm events that occurred in spring 2021. The results show that position error significantly degraded dust forecasting was evaluated against two severe dust storm cases from spring 2021, demonstrating that position errors notably deteriorated forecast performance in terms of RMSE and NMB Root

Mean Square Error (RMSE) and Normalized Mean Bias (NMB), impeding the EnKF's effective assimilation. Conversely, and hindered the EnKF from assimilating valid observations. In contrast, the VTS-EnKF yielded substantial improvements in both dust analysis fields and forecasts improved both the analysis and forecast accuracy compared to the EnKF, conventional EnKF. Additionally, to provide a more rigorous assessment of its performance, experiments were conducted using fewer ensemble 25 members and different time intervals.

## 1 Introduction

Dust storms are a natural meteorological disaster (Zhang et al., 2005), whose occurrence is attributed to frequent strong winds over dry and loose soil texture (An et al., 2018). Dust particles can be lifted up to a few miles and transported over, identified as natural meteorological disasters, are phenomena closely associated with the prevalence of potent winds over arid regions 30 with a loosely packed soil composition (Zhang et al., 2005; An et al., 2018). These storms enable dust particulates to ascend to remarkable heights, traversing distances of thousands of kilometers away (Zhang et al., 2018), with dust aerosol concentrations as high as thousands of  $\mu\text{g m}^{-3}$  (She et al., 2018). Meanwhile, with documented aerosol concentrations soaring to thousands  $\mu\text{g m}^{-3}$  (She et al., 2018). During transportation, these aerosols can interact with  $\text{SO}_x$  and  $\text{NO}_x$  undergoing heterogeneous chemical reactions during transportation, leading to further severe further participate in heterogeneous chemical reactions with 35  $\text{SO}_x$  and  $\text{NO}_x$ , exacerbating the severity of aerosol pollution (Song et al., 2022). These pose a great threat to human health by causing damage to the, thereby significantly endangering human health through respiratory and circulatory systems system impairments (Gross et al., 2018; Goudie, 2014). East Asia, as one of the major dust sources and affected regions a dominant 40 source and recipient of dust activity (Hu et al., 2019), has drawn much attention from researchers. For instance, in the 2021 spring, witnessed intensified scholarly focus. Notably, the spring of 2021 observed the onslaught of several super dust storms, which are recorded as the largest ones in terms of intensity and coverage in a decade (Filonchyk and Peterson, 2022), swept 45 over East Asia and caused huge loss of lives and properties both in unprecedent in intensity and geographical span over the past decade (Filonchyk and Peterson, 2022)—resulting in substantial life and property losses across Mongolia and China (Gui et al., 2022; Jin et al., 2022; Tang et al., 2022). An accurate early warning of Consequently, the imperative for an accurate and timely forecasting system to dust storms is, therefore, in essential need to help minimize the damages accentuated, aiming to mitigate their detrimental impacts.

The growing interest in dust storms from the public has stimulated the understanding of the physical processes associated with the dust cycles over the past decades. To achieve the simulation of dust storms, several In recent years, heightened public concern has fueled advancements in deciphering the physical mechanisms governing dust cycle dynamics, leading to significant strides since the 1990s. To accurately replicate dust storm behavior, numerous dust emission parameterization 50 schemes have been proposed since the early 1990s, e.g., devised, including MB95 (Marticorena and Bergametti, 1995), Shao96 (Shao et al., 1996; Shao, 2004), Zender03 (Zender et al., 2003), and the more recent K14 (Kok et al., 2014). Coupled with Integrated within chemical transport models, dust simulations could then be carried out, e.g., these frameworks facilitate dust storm modeling exercises, exemplified by systems such as CUACE/DUST (Chinese Unified Atmospheric Chemistry

Environment for Dust) (Gong and Zhang, 2008), BSC-DREAM8b (Dust Regional Atmospheric Modeling) (Pérez et al., 55 2006; Mona et al., 2014), GEOS-Chem (Duncan Fairlie et al., 2007), and LOTOS-EUROS (Timmermans et al., 2017; Manders et al., 2017). These ~~dust models help evaluate health effects, quantify Earth system impacts, and reveal the synoptic climatic driving forces, and also to build dust models are instrumental in assessing health hazards, quantifying the planet's ecosystem responses, elucidating large-scale climate drivers, and, importantly, informing the development of~~ early warning systems ~~via reporting the dust loading in the few hours to few days. However, various numerical approximations are used~~ 60 ~~to solve the dynamic dust equations, so that the model configuration (like coarse grid cell and time step), uncertain input data (e.g., wind field and boundary/initialconditions) inevitably limit the model forecast skill (Mallet and Sportisse, 2006).~~ Notably, it is widely accepted that ~~uncertainty in the emission parameterization is the largest error source of dust simulation (Ginoux et al., 2001, 2012; Di Tomaso et al., 2017, 2022; Jin et al., 2019a, b). The performance capable of predicting imminent~~ 65 ~~dust loads within timescales ranging from hours to days. Despite these advancements, the forecast skill of such models remains constrained by inherent uncertainties tied to input variables—such as wind velocity fields and initial/boundary conditions—as well as computational approximations necessitated by coarse spatial and temporal resolutions (Mallet and Sportisse, 2006).~~ Of particular note, the scientific consensus highlights the emission parameterization uncertainty as the paramount source of error in dust storm simulations (Ginoux et al., 2001, 2012; Di Tomaso et al., 2017, 2022; Jin et al., 2019a, b). Consequently, the predictive prowess of numerical dust models ~~degrades greatly due to these factors~~ is notably compromised under the weight 70 ~~of these combined limitations.~~

~~Observation is another fundamental method for exploring Observational studies constitute another pivotal approach in elucidating the intensity and spatial distribution dispersion of dust storms (Muhammad Akhlaq et al., 2012). Satellite-based observations are a rapidly developing technology that is widely used in detecting dust storms (Gui et al., 2022). Products from satellites such as Among these, satellite-based monitoring technologies have rapidly evolved into a prevalent tool for dust~~ 75 ~~storm detection, offering expansive and detailed insights (Gui et al., 2022). Platforms like MODIS, Himawari, and Fengyun-4A provide various information about aerosol properties with deliver a wealth of data on aerosol characteristics, characterized by high spatial resolution and extensive coverage. However, they only retrieve column-cumulative values and are easily affected by clouds and other particles. Therefore, significant global coverage. Nonetheless, these satellite products aggregate column-integrated information and are prone to interference from cloud cover and other atmospheric constituents, thereby~~ 80 ~~introducing substantial uncertainties and biases exist, and pre-processing is necessary before they can accurately represent dust load (Jin et al., 2019b, 2022). Ground-based observation networks, on the other hand, are highly reliable and have high into dust load estimates. Consequently, preprocessing is imperative to ensure their reliability in depicting actual dust concentrations (Jin et al., 2019b, 2022). Concurrently, ground-based observational networks, known for their reliability and fine temporal resolution, making them indispensable for measuring dust aerosol concentration (She et al., 2018). In recent years, China has~~ 85 ~~invested heavily in the construction of a ground station network, and there are now over 1600 ground stations throughout China that provide a comprehensive picture of dust plumes (Gui et al., 2022). The play a crucial role in precisely measuring aerosol concentrations (She et al., 2018). China, in particular, has made substantial investments in constructing its ground monitoring infrastructure, establishing an expansive network comprising over 1,600 stations nationwide. This dense grid of ground stations~~

furnishes a granular view of dust plume dynamics across the region (Gui et al., 2022), enriching the dataset for examining East Asian dust storms and reinforcing the national observation network provides rich measurements for investigating dust storms in East Asia's capacity for comprehensive dust research.

Data assimilation is a powerful technique that integrates models and observations. Based on Bayesian theory, data assimilation algorithm is intended to calculate the posterior probability distribution of the model state given the observations as accurately as possible (Law and Stuart, 2012). Two main approaches to data assimilation are variational methods and filtering methods. Variational methods, such as stands as a potent methodology that harmoniously merges model with observations. Rooted in Bayesian principles, its objective is to ascertain the most plausible model state posterior, given the available observations, through probabilistic estimation (Law and Stuart, 2012). The realm of data assimilation encompasses two principal methodologies: variational techniques and filtering algorithms. Variational methodologies, exemplified by 4DVar, aim to retrieve an optimal posterior analysis that fits both the prior and measurements over a time window by minimizing a strive to determine an optimal analysis that reconciles both prior knowledge and observational constraints over a defined temporal span, achieved by optimizing a predefined cost function (Rabier and Liu, 2003). Variational methods are widely used in inverse modeling of These methods are prominently employed in tasks such as inverse modeling for initial conditions and emission fields (Jin et al., 2022; Bergamaschi et al., 2010; Corazza et al., 2011) and reanalysis data, but they require tangent linearization or adjoint of the model, which can be challenging to develop and maintain. The cost function minimization is computationally demanding, especially for high-dimensional and nonlinear models. Filtering methods, on the other hand, as well as in reanalysis endeavors. However, their implementation hinges on the often intricate development and maintenance of tangent linear or adjoint model forms. Furthermore, the computational burden associated with minimizing the cost function escalates dramatically with the complexity and dimensionality of the models. Conversely, filtering methodologies assimilate observations sequentially and are more efficient for operational forecasting systems. Various filtering approaches, such as, aligning them favorably with operational forecasting frameworks. This class includes the Kalman Filter (Kalman, 1960), its extension in the Extended Kalman Filter (Brunner et al., 2012), and the more sophisticated Particle Filter (Leeuwen et al., 2019), have been developed. Among all the filtering methods, the . Prominent among these is the Ensemble Kalman Filter (EnKF) is the most popular filtering method due to its ability to handle distinguished for its adeptness at managing high-dimensional models, easy parallelization (Evensen, 1994; Katzfuss et al., 2016; Houtekamer and Zhang, 2016). It uses limited ensembles to estimate the systems, amenability to parallel computation (Evensen, 1994; Katzfuss et al., 2016; Houtekamer and Zhang, 2016), and reliance on ensemble members to infer background error covariance statistics of the model structures (Hamill, 2006; Houtekamer et al., 2014). Its advantages include handling non-linearity, not requiring explicit calculation of tangent linear operators virtues encompass nonlinearity accommodation, dispensing with the necessity for explicit tangent linear calculations, and computational efficieney (Bannister, 2017). EnKF has been successfully applied in various disciplines, e.g., weather forecasting (Houtekamer et al., 2005) and hydrology (Reichle et al., 2002). Meanwhile, inherited from Kalman filter, EnKF relies on Gaussian distribution of error statistics (Amezcua and Van Leeuwen, 2014). For efficacy (Bannister, 2017), rendering it a favored tool across domains, including weather prediction (Houtekamer et al., 2005) and hydrological studies (Reichle et al., 2002). Despite these strengths, the EnKF, as an extension of the Kalman Filter, presumes Gaussian error distributions (Amezcua and Van Leeuwen, 2014)

125 . When dealing with non-Gaussian ~~problems~~~~error statistics~~, EnKF can create suboptimal ~~results~~~~outcomes~~ for the linearized dynamics or operators and sampling errors caused by finite ensemble members (Lei et al., 2010).

The primary source of uncertainty in dust simulation is related to the online emission parameterization. Therefore, most previous studies on dust storm data assimilation have focused on emission inversion. For example, Yumimoto and Takemura (2015) used MODIS AOD retrievals for long-term dust emission inverse modeling over Asia. Escribano et al. (2017) investigated the impact of five different satellite AOD products on dust emission. Uncertainty in dust storm modeling predominantly stems from the real-time estimation of dust emissions, leading to a research emphasis on emission inversion through data assimilation techniques. Studies such as those conducted by Yumimoto and Takemura (2015) leveraged long-term MODIS Aerosol Optical Depth (AOD) retrievals for emission inversion across Asia. Similarly, Escribano et al. (2017) underscored the varying impact of distinct satellite AOD datasets on emission inversions over northern Africa and the Arabian Peninsula. Their results indicated that the assimilation outcome is more sensitive to model uncertainties than to observational uncertainties in some cases. The uncertainties in model actually have a greater impact in the assimilation results. In recent studies, we have carefully explored the variability determining assimilation outcomes. Building upon this foundation, recent investigations have delved deeper into the intricacies of dust emission over the Mongolia and China Gobi desert by assimilating ground-based variability in the Mongolian and Chinese Gobi deserts. This includes the assimilation of ground-level PM<sub>10</sub> ~~econcentration~~ concentrations (Jin et al., 2018), polar-orbiting MODIS satellite data (Jin et al., 2022), and geostationary Himawari-8 AOD measurements (Jin et al., 2019b). To effectively improve dust storm emission inversion, we introduced refine emission inversion processes, innovations like observation bias correction (Jin et al., 2019a), adjoint-based emission source tracking (Jin et al., 2020), and grid distortion (Jin et al., 2021). These works provide valuable insights into the dynamics adjustment methodologies (Jin et al., 2021) have been introduced, significantly advancing our understanding of dust emission and quantify their impacts on the environment and climate. However, little attention has been paid to dynamics and their environmental and climatic implications. Despite these advancements, the application of high-quality dust storm sequential forecasting using filter methods. Recently sequential forecasting methodologies utilizing filtering techniques for dust storms has received limited exploration. To address this gap, we have developed a data assimilation-based recently engineered an operational dust forecasting system by coupling framework that integrates Ensemble Kalman Filter (EnKF) and Localized Ensemble Kalman Filter (LEnKF) assimilation algorithms with a chemical transport model (with the LOTOS-EUROS) through an interface of our self-designed assimilation toolbox model. This integration is facilitated by our custom assimilation software, Pyfilter (Pang, last access: May. 2024). We tested this system on the super dust storms that occurred in the spring of Testing this system against the backdrop of the record-breaking dust storms of spring 2021, as we will show later. Significant improvements were found in the assimilation analysis and assimilation-based forecasts compared to the pure model results. Furthermore, the LEnKF algorithm with a proper localization distance threshold was consistently shown to be superior to the EnKF algorithm has demonstrated marked improvements in both the assimilated analyses and forecast results compared to standalone model forecasts. Notably, when configured with an appropriate localization radius, it consistently outperformed the EnKF, highlighting the potential for localized filters in enhancing the precision of dust storm forecasting.

Despite the positive results obtained from our tests, there are still unresolved errors. One major issue is the apparent mismatch between the observations and model in space after encouraging outcomes of our experimental assessments, several challenges persist, chief among them being a spatial misalignment between model forecast and observations following long-distance transport. In addition to the discrepancy in the dust intensity dust transport. This disparity not only encompasses discrepancies in the estimated dust intensity but also manifests in inaccuracies regarding the timing of dust arrival and departure, as will be illustrated elaborated in Sect. 2.4, the timing of the dust arrival and departure reported by the model simulation also differs heterogeneously from reality. The dust intensity is a key feature, as well as the position, when evaluating a dust forecast. The former represents the actual dustload. In the context of dust storm forecasting evaluation, both the intensity and the position accuracy of the dust plume are paramount. Intensity directly correlates with the amount of airborne dust, while the latter reveals position is vital for understanding where the dust plume affects at a given instant. For an operational forecasting and warning system, the position information is sometimes more important than the intensity. In terms of mathematical metrics, such as systems, pinpointing the correct location of impending dust impacts can carry even greater urgency than estimating dust load precisely. Quantitatively, these spatial mismatches significantly deteriorate the forecast performance when evaluated using conventional measures like the root mean square error, the forecasting skills degraded significantly with the presence of the position mismatch. The detailed mechanism behind this issue and its further consequences will be illustrated in Section (RMSE). The underlying causes of this spatial discrepancy and its broader ramifications on forecasting efficacy will be meticulously examined in Sect. 3.2.

The so-called phenomenon labeled as "position error" in dust aerosol simulations typically arises after emerges following long-distance transport. There are many factors that contribute to the position error, such as simplified physical processes, coarse model resolution, uncertain This error is multifaceted, stemming from a constellation of factors including the simplification of physical processes in models, coarse spatial and temporal resolutions, indeterminate values of physical parameters (Rav-180 elia et al., 2007), and the uncertainty in the meteorological field and emission timing, as illustrated in our previous work (Jin et al., 2021). Similar to the uncertainties inherent to both meteorological inputs and the precise timing of dust emissions, as we previously highlighted (Jin et al., 2021). Resembling the issues encountered in dust emission inversion studies discussed above, the deviations between the model, discrepancies between model forecast and observations in dust storm data assimilation are also attributed to the uncertainty in the dust emission efforts can also be traced back to uncertainties in dust emission 185 estimates, where ensemble individuals are generated with perturbed dust emission fields. However, the uncertainty in the dust plume position is difficult to quantify and is hardly taken into account when designing simulations incorporate varied emission scenarios. The challenge lies in the quantification of position error and its subsequent inaccurate formulation of the background error covariance of the simulated dust plume. Therefore, classic dust data assimilation methodologies now focus on intensity adjustment and are not capable of handling the imbalanced uncertainties between the observations and simulation caused by the 190 matrix. Consequently, EnKF calibrates both intensity and position error, while it cannot handle position errors if the ensemble is under-dispersive with regard to position. This deficiency curtails the capacity of current assimilation methodologies to correct position error.

Position error is not a mere occasional issue, but rather a cumulative error that accompanies model simulations over time. This type of error is quite common in forecasting phenomena—an occasional issue. Instead, it is a error that accumulates as simulations progress, plaguing forecasts such as hurricanes, dust storms, convective thunderstorms, and precipitation (Dance, 2004; Nehrkorn et al., 2015; Jin et al., 2021). However, there efforts explicitly targeting the mitigation of this error have been relatively few studies aiming to address this problem. Brewster (2003) proposed an objective method for identifying and correcting position errors using densely distributed and scarce. One pioneering study by Brewster (2003) outlined an objective methodology to pinpoint and rectify position errors leveraging a wealth of high-resolution, densely deployed observational data. Their research demonstrated that it is possible to correct position errors findings in Observing System Simulation Experiments (OSSEs) affirmed the feasibility of correcting positiona errors. Jin et al. (2021) developed a grid-distortion technique based on image morphing and grid distortion strategy grounded in image morphing techniques for post-processing, which successfully realigned effectively realigning modeled dust plumes to better match the measurements. Both of these improvements rely on densely distributed observations, but often the observations do not fully cover the entire domain, limiting the applicability of these methodsconform more closely with observations. While these enhancements underscore the potential for addressing position errors, their efficacy hinges critically on the availability of a comprehensive and closely spaced observational network. Regrettably, in many practical scenarios, observational coverage is patchy and incomplete, curtailing the broad application of these corrective measures.

In this paper, the standard EnKF assimilation EnKF is coupled with a valid time shifting Valid Time Shifting (VTS) method (Xu et al., 2008; Lu et al., 2011; Zhao et al., 2015; Huang and Wang, 2018) for better resolving the position error strategy, referred to henceforth as VTS-EnKF, specifically tailored to mitigate position errors prevalent in long-distance dust storm transportsimulation. This assimilation methodologyis referred to as. The VTS methodology, inspired by prior works such as Xu et al. (2008); Lu et al. (2011); Zhao et al. (2015); Huang and Wang (2018), augments the EnKF by incorporating temporal flexibility to better align simulated dust plumes with observations. In practice, the VTS-EnKF throughout this paper. For assimilation analysis at a given time, the enhances the background error covariance of the simulated dust plume is calculated using not only the original ensemble simulation, but also the same ensemble simulations at neighboring moments (a few hours earlier and later) (Gasperoni et al., 2022, 2023). These extra ensemble members represent the potential position spread of the actual dust plume, effectively accounting for transport errors. The resampled ensemble members quantify the complex covariancee that captures both intensity and position error dynamics, without requiring additional processing on estimation for each assimilation cycle by considering not solely the immediate ensemble members but also those from neighboring time points, slightly before and after the target moment (Gasperoni et al., 2022, 2023). By doing so, this approach encapsulates a broader range of potential dust plume positions, thereby inherently compensating for transport-related inaccuracies without necessitating intricate adjustments to observations, meteorological fieldsinputs, or other underlying physical parameters. We tested The efficacy of the VTS-EnKF on-was assessed against two severe dust storm events that occurred in 2021. Our results show superior assimilation performance compared to the standard findings underscore the substantial improvement offered by this hybrid method over pure EnKF, particularly when in scenarios where significant position errors are present in the

~~simulated dust plume evident in model prior. This advancement paves the way for more precise and temporally coherent dust storm forecasting, especially amidst the complexities of long-distance transport.~~

This paper is organized as follows: Section 2 introduces the dust measurements and dust model used in the research. We also 230 discuss that the major uncertainty of dust model forecast comes from the emission. But there is another problem: position error that remains to be solved. Then in Sect. 3, we explain introducing the procedure of ensemble-based assimilation algorithm and the mechanism of position error's negative effect on EnKF. How the new assimilation method works is explained in detail afterwards. To test the performance of EnKF with VTS, sequential assimilation experiments on several dust storm events are 235 designed. Section 4 analyses the results of experiments in terms of both the assimilation analysis and forecast performance. Section 5 concludes this paper.

## 2 ~~Dust measurement~~observation, model and position error

In this paper, ground-based PM<sub>10</sub> is used as the ~~measurement with~~dust observation to be assimilated after a bias-correction procedure to remove the non-dust part. The dust model adopted is the LOTOS-EUROS. Considering the model processes, the greatest uncertainty in the dust simulation comes from uncertainty the emission parameterization. Meanwhile, uncertainties 240 from meteorology can also influence the model forecast and lead to the "Position error".

### 2.1 ~~Dust measurements~~Ground PM<sub>10</sub> observations

Thanks to the continuous efforts and investments from the Ministry of Ecology and Environment, over 1600 ground monitoring 245 stations have been established across China, with some locations in northern China shown in Fig. 1. These stations provide real-time hourly air quality data, and their hourly PM<sub>10</sub> concentrations serve as indispensable datasets for measuring dust load, which are used as observations to be assimilated in this paper.

Despite the advantages of low uncertainty and high time resolution, PM<sub>10</sub> observations are not assimilated directly due to the mixed state of dust and non-dust aerosols in the original PM<sub>10</sub> data. Anthropogenic activities, such as vehicle emissions, coal burning, and industrial processes (Wu et al., 2018; Liu et al., 2018), along with natural sources like volcanic eruptions, sea spray, wildfires, and wind-blown dust contribute to the total PM<sub>10</sub> concentration. Assimilating PM<sub>10</sub> data directly into a 250 dust model may introduce ~~biased errors~~biases and lead to model divergence (Jin et al., 2019a). Therefore, it is necessary to eliminate the bias before data assimilation.

In this study, the non-dust portion of PM<sub>10</sub> is approximated through a separate model. The dust observations assimilated are calculated by subtracting the non-dust fraction from the original PM<sub>10</sub> measurements. Further details regarding the baseline removal (BR) can be found in Jin et al. (2022).

### 255 2.2 Dust model

In this paper, the LOTOS-EUROS v2.1 is used to simulate dust storms that occurred in East Asia. Originating from the Long-Term Ozone Simulation (LOTOS) and the European Operational Smog model (EUROS) in the 1980s, LOTOS-EUROS has

undergone continuous development for various applications. It has been widely used in air quality forecasting (Curier et al., 2012; Brasseur et al., 2019; Lopez-Restrepo et al., 2020; Skouliidou et al., 2021), dust/aerosol emission inversion (Yarce Botero et al., 2021; Jin et al., 2018, 2019a, b, 2021, 2022), and source apportionment (Kranenburg et al., 2013; Timmermans et al., 2017; Pommier et al., 2020; Jin et al., 2020). In spring 2021, several super dust storm events occurred in East Asia, around 15th March, 28th March. These events, referred to as DSE1 and DSE2, are used as test cases in this study. These dust storms caused significant losses in both Mongolia and China (Jin, 2021; Chen and Walsh, 2021). Accurate forecast of such severe sandstorms is crucial for reducing health and property damages.

To simulate the dust storm over East Asia, LOTOS-EUROS is configured following our recent work (Jin et al., 2022): The simulation domain is from 15° N to 50° N and 70° E to 140° E with a grid resolution of  $0.25^\circ \times 0.25^\circ$ . The model consists of 8 layers with a top at 10 km. The boundary conditions are set to zero assuming that all the dust aerosols are emitted during the simulation window. Dust emission, deposition, advection, diffusion and dry/wet deposition are considered within the model. The model output is at the interval of 1 hour.

The whole model simulation period is set from 13 to 17 March for DSE1 and 27 to 30 March for DSE2, which covering the whole life cycles of emission and long-distance transport. More details could be found in Jin et al. (2022).

### 2.3 Uncertainties from emission and meteorology

The goal of this study is to calculate the dust concentration field that best fits both the a priori and observations at each assimilation analysis. The optimized field will then be used as the initial condition for sequential dust forecasts, as explained in Section 3.1. It is essential to define and quantify the uncertainty in dust simulations. As previously mentioned, the uncertainty in emission parameterization is widely believed to be the dominant error source in dust simulation (Ginoux et al., 2001, 2012; Di Tomaso et al., 2017, 2022; Jin et al., 2019a, b). High levels of uncertainty in dust emission parameterization arise from insufficient knowledge about windblown erosion, lack of accurate input on soil characteristics, and the models' inability to resolve the fine-scale variability in wind fields governing dust emission (Escribano et al., 2017; Foroutan et al., 2017; Foroutan and Pleim, 2017; Jin et al., 2019b).

In our recent work (Jin et al., 2022), a 4DVar-based inverse modeling approach was employed to retrieve an optimal emission field for the three major dust storms in spring 2021 (Jin et al., 2022). The a priori emission,  $f_{\text{priori}}$ , followed the *Zender03* dust emission parameterization scheme (Zender et al., 2003). To compensate for potential errors, a spatially varying multiplication factor was introduced. Mathematically, it was quantified by a background error covariance matrix,  $\mathbf{B}$ , to describe the potential spread of the actual dust emission flux.

Another source of the uncertainties arises from the meteorological field. In our previous papers, uncertainties from meteorology and the position error were neither taken into account (Jin et al., 2022; Pang et al., 2023). In this paper, European Center for Medium-ranged Weather Forecast (ECMWF) ensemble forecast (totally 51 ~~ensembles~~ensemble members) are used. Each one of the model ~~ensembles~~ensemble members is driven by one unique ensemble meteorology field. N=32 ensemble meteorological fields are randomly selected. Its grid resolution is about 14 km. The 6-hourly short-term meteorological forecast field is interpolated to hourly values. The grid resolutions are also averaged to fit the model resolution.

In general, we assign the dust simulation uncertainty to both emission and meteorology. Ensemble emission field  $[\mathbf{f}_1, \dots, \mathbf{f}_N]$  are generated randomly following the emission uncertainty choice  $\mathbf{f}_{\text{priori}}$  and  $\mathbf{B}$  in Jin et al. (2022). Meteorologic field  $[\mathbf{w}_1, \dots, \mathbf{w}_N]$  are randomly selected from the total 51 ensemble meteorology. They are used to forward the LOTOS-EUROS 295 model  $\mathcal{M}$  for the ensemble dust simulations  $[\mathbf{x}_1, \dots, \mathbf{x}_N]$  as:

$$[\mathbf{x}_1, \dots, \mathbf{x}_N] = [\mathcal{M}(\mathbf{f}_1, \mathbf{w}_1), \dots, \mathcal{M}(\mathbf{f}_N, \mathbf{w}_N)] \quad (1)$$

N refers to the total ensemble number, and the choice will be explained in Section 3.3.

These ensemble individuals are used in the EnKF assimilation for representing the covariance dynamics of the dust plume, which resulted in more accurate dust analysis and forecast as will be shown in Sect. 4. However, the ensemble realizations 300 mainly represent the uncertainty in the intensity feature, and hardly help resolve the positional deviation between the observation and simulation. The presence of position error would give rise to a divergent assimilation analysis as will be illustrated in Sect. 3.1.

## 2.4 Position error

For all the dust events, most of the dust particles were originated from the Mongolia Gobi desert, and carried by the prevailing 305 wind towards southeast. After several thousands of kilometers transport which lasted about one to two days, they finally arrived in the densely-populated northern China.

Position errors are clearly visible in the simulation of two dust events (DSE1 and DSE2). Examples can be best seen in Fig. 1, which plots the evolution of LOTOS-EUROS simulated surface dust concentration alongside BR- $\text{PM}_{10}$  (BR: non-dust 310 baseline-removed) concentration observations for DSE1 (panel a) and DSE2 (panel c). The corresponding standard deviations from ensemble model simulations and the model-minus-observation differences (absolute values) are also plotted in panel b and panel d. In panel a.1, the model generally simulates a similar shape of the dust plume as indicated by the observations at the first instance, though the dust load intensities differ to some extent. However, during the subsequent transport, positional errors arise gradually. In panel a.2, the right part of the simulated dust plume is positioned about 100 to 200 km too far south compared to ground-based observations. Consequently, the Root Mean Square Error (RMSE) increases significantly from 587.83  $\mu\text{g m}^{-3}$  315  $\mu\text{g m}^{-3}$  at 8:00 to 856.36  $\mu\text{g m}^{-3}$  at 11:00. This position error continues to accumulate over the following 3 hours at 14:00. The development of position errors is further clearly visible against the  $\text{PM}_{10}$  observations, especially in the light blue box in panel a.3. The model simulation missed all the dust load there, while the observations indicate a significant amount of dust aerosols. It can also be seen in panel b.3 that the model-minus-observation differences exceed 1000  $\mu\text{g m}^{-3}$  320  $\mu\text{g m}^{-3}$  there. Similarly, for DSE2 occurring on 28th March, 2021, as shown in Fig. 1(c), discrepancies between observations and simulation become more explicit as time evolves, especially for the dust in the light blue box in panels c.1 and c.2. The RMSE remains high from 542.15  $\mu\text{g m}^{-3}$  at 8:00 to 479.6  $\mu\text{g m}^{-3}$  at 11:00, and this error expands to a wider extent as shown in the enlarged green box in panel c.3. This position error not only limits the pure model forecast performance but also significantly degrades the subsequent assimilation analysis and forecast. With an ensemble-approximated background

covariance unrepresentative of position error, neither the position deviation nor the intensity deviation can be fully resolved, as  
325 will be explained in Sect. 3.2.

Potential sources of position error in dust model may be attributed to inaccuracies in emission timing, uncertainties in meteorological input data (e.g., wind fields responsible for transporting dust plumes from the Gobi Desert in Mongolia and China to downwind regions), or a combination of these factors. Adjusting the emission timing profile, which characterizes the release of soil particles into the atmosphere, could partially correct the position of the dust plume. Moreover, alterations in meteorological conditions governing long-distance transport might also realign the dust plume's position. To address the position error, a comprehensive covariance matrix is necessary to account for both the potential variations in emission temporal profiles and the accumulation of uncertainties along the plume's extensive trajectory. Concurrently, a significantly larger ensemble size is required to propagate these uncertainties, featuring high degrees of freedom, into the  $PM_{10}$  observational space. Although a sophisticated covariance matrix and a substantial ensemble size (resulting in considerable computational cost) may aid the  
330 EnKF in simultaneously resolving position and intensity errors, this approach is often prohibitively expensive. Therefore, an efficient and cost-effective alternative solution is required.

### 3 Assimilation methodology and experiments

EnKF is a powerful algorithm to tune the model simulation with observations especially in intensity adjustment given the perturbed emission spreads. However, when faced with the position error, its weakness is exposed that some model-minus-  
340 observation inconsistency cannot be resolved by EnKF as illustrated in Section 3.1. On the contrary, our EnKF with VTS can correct both the position error and the intensity. Assimilation strategy is designed and embeded into a assimilation forecast system in Section 3.2. Experiments are designed on the dust storms occur in spring, 2021, which are illurtated in Section 3.3.

#### 3.1 EnKF

The Ensemble Kalman Filter (EnKF) was first proposed by Evensen (1994). Stemming from the Kalman Filter, it was designed  
345 to address high-dimensional problems by employing limited ~~ensembles ensemble members~~ to approximate the true background error covariance. It relies on the Gaussian distribution of errors. The EnKF has been proven to be practical and efficient in various applications, particularly in sequential forecasting with the aid of localization (Lopez-Restrepo et al., 2020; Park et al., 2022). In any sequential forecast system, the objective of assimilation analysis is to provide an optimized initial state or parameter field, which, in this study, corresponds to the 3D dust concentration. This is achieved by assimilating the available  
350 measurements. The estimated dust concentration field can then be used to onward the model for more accurate dust forecasting.

Here we use the stochastic EnKF formulated by Burgers et al. (1998). It features the ~~pertubated~~ ~~perturbated~~ observations to maintain a reliable ensemble spread. Starting from the prior dust concentration field  $\mathbf{x}_t^{f,i}$  at time  $t$  which is calculated by model integral operator  $\mathcal{M}$  from the dust concentration field at the previous time step  $\mathbf{x}_{t-1}^{a,i}$ .

$$\mathbf{x}_t^{f,i} = \mathcal{M}(\mathbf{x}_{t-1}^{a,i}, \mathbf{f}^i, \mathbf{w}^i) \quad (2)$$

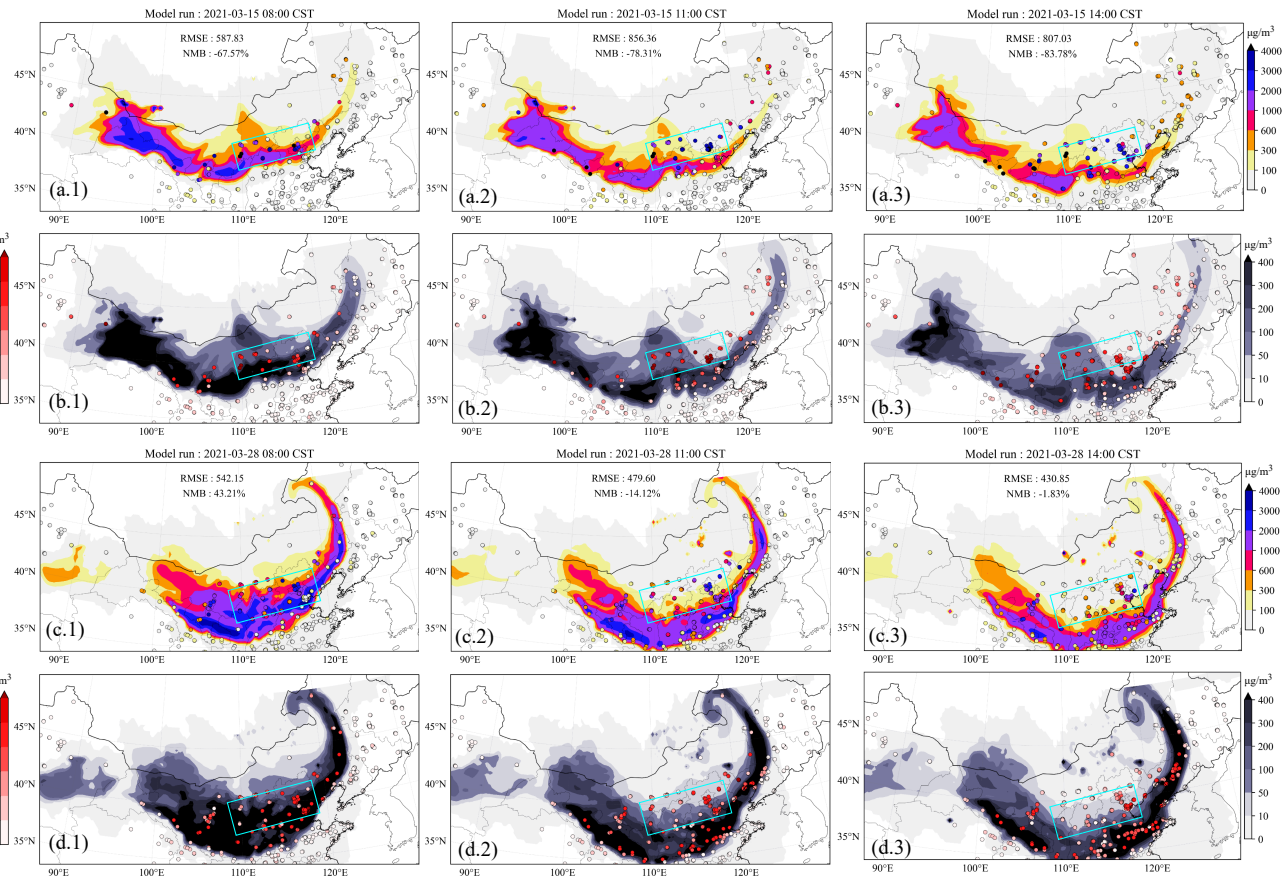


**Figure 1.** Evolution of the simulated dust plume from average of 32-model ensembles with scatter of ground BR-PM<sub>10</sub> observations ensemble members (a.1-3). Their corresponding standard deviation from model ensembles with scatter of the model-minus-observation differences ensemble members (absolute value) (b.1-3) at 08:00, 11:00 and 14:00 15th March, 2021, respectively. Figures below are the same except the time is at 05:00 (c.1 and d.1), 08:00 (c.2 and d.2), 11:00 (c.3 and d.3) 28th March, 2021, respectively. The filled circles represent ground BR-PM<sub>10</sub> + baseline-removed PM<sub>10</sub> observations in (a) and (c), and the model-minus-observation differences (absolute value) at various observation sites in (b) and (d). The colorbar in panel a and c represents the concentrations, and the colorbar in panel b and d represents the model-minus-observation differences (left) and standard deviation (right). BR-PM<sub>10</sub>: baseline-removed PM<sub>10</sub>, CST: China Standard Time.

$$\mathbf{X}^f = [\mathbf{x}_t^{f,1}, \mathbf{x}_t^{f,2}, \dots, \mathbf{x}_t^{f,N}] \quad (3)$$

Note that for the first analysis the prior dust simulation are extracted from the model with the perturbed emissions as shown in Eq. 1. The  $i$  represents the ensemble individual number.  $N$  is the number of ~~ensembles~~ensemble.  $\mathbf{X}^f$  is the ensemble model simulation matrix consists of the whole ensemble individuals.

360 The ensemble perturbation matrix  $\mathbf{X}^{f'}$  calculates the deviation between the ensemble individuals  $\mathbf{x}_t^{f,i}$  and the ensemble mean state  $\bar{\mathbf{x}}_t^f$ .

$$\bar{\mathbf{x}}_t^f = \frac{1}{N} \sum_{i=1}^N \mathbf{x}_t^{f,i} \quad (4)$$

$$\mathbf{X}^{f'} = [\mathbf{x}_t^{f,1} - \bar{\mathbf{x}}_t^f, \mathbf{x}_t^{f,2} - \bar{\mathbf{x}}_t^f, \dots, \mathbf{x}_t^{f,N} - \bar{\mathbf{x}}_t^f] \quad (5)$$

365 Then the background error covariance matrix  $\mathbf{P}^f$  is approximated by  $\mathbf{X}^{f'}$  as follows:

$$\mathbf{P}^f = \frac{1}{N-1} \mathbf{X}^{f'} \mathbf{X}^{f'\top} \quad (6)$$

Afterwards, the Kalman gain  $\mathbf{K}$  can be calculated with  $\mathbf{P}^f$  and  $\mathbf{O}$ .

$$\mathbf{K} = \mathbf{P}^f \mathcal{H}^T (\mathcal{H} \mathbf{P}^f \mathcal{H}^T + \mathbf{O})^{-1} \quad (7)$$

370  $\mathbf{K}$  weights the increments given from the observations to the prior estimation. In this paper, they are the BR-PM<sub>10</sub> observations stored in  $\mathbf{y}$  and dust simulation stored in vector  $\mathbf{x}$ .  $\mathcal{H}$  is the observation operator which maps the model states into the observational space.

375  $\mathbf{O}$  is the observational error covariance matrix that weights the uncertainty of the measurements. In this case, it is the uncertainties from ground-based BR-PM<sub>10</sub> concentrations.  $\mathbf{O}$  is defined as follows: the minimum uncertainty threshold is set to be 200 ~~μg m<sup>-3</sup>~~Root of error from observations  $\mu\text{g m}^{-3}$  Standard deviation of observation error below the threshold is set to be 200 ~~μg m<sup>-3</sup>~~μg m<sup>-3</sup> and those over it is set to be  $200 + (\mathbf{y} - 200) \times 0.2 \mu\text{g m}^{-3}$ . This definition can prevent the posteriori from getting too close to the low value observations and thus leading to model divergence.  $\mathbf{O}$  is a diagonal matrix assuming that all the observations are independent.

In the end, the posteriori estimation individual  $\mathbf{x}_t^{a,i}$  can be updated as follows:

$$\mathbf{x}_t^{a,i} = \mathbf{x}_t^{f,i} + \mathbf{K}(\mathbf{y} + \boldsymbol{\epsilon}^i - \mathcal{H}\mathbf{x}_t^{f,i}) \quad (8)$$

380  $\boldsymbol{\epsilon}^i$  represents the sampling error vector. It is a random vector subjecting to normal distribution. Its mean is 0 and covariance is the root of diagonal from  $\mathbf{O}$ .

The equations presented above describe the Ensemble Kalman Filter (EnKF) algorithm for dust storm assimilation, which focuses on intensity adjustment. The EnKF assimilation aims to compute an optimal posteriori estimation given a priori information and observations. It is highly dependent on the observations and the ensemble spread. In fact, the ensemble-based

385 background covariance matrix,  $\mathbf{P}^f$ , utilizes the ensemble members to approximate the true background covariance. The spatial distribution of the standard deviation (square root of the diagonal values in  $\mathbf{P}^f$ ) from 32 model ~~ensembles~~ensemble members, along with the scatter of absolute model-minus-observation differences in two cases (DSE1, DSE2), is shown in Fig. 1 (b,d). In general, their spatial distribution corresponds well to the simulated dust field depicted in Fig. 1 (a, c). Concurrently, the uncertainty in the light blue box decreases rapidly as the simulated dust plume moves southward, as illustrated in panels b.1 390 and b.2. This suggests that our ensemble model simulations are highly confident that there are less affected by dust aerosols. However, the observations indicate that this area remains heavily polluted. In the case of DSE2, the situation becomes more complex. The simulated dust plume in DSE2 covers most of the observation area with a high dust load, as demonstrated in panels c.1 and d.1. The uncertainty, on the other hand, reveals that the ensemble model is less confident about the dust load, especially in the light blue box displayed in panel d.2. After 3 hours, these discrepancies become more evident. The extent to 395 which this situation affects the EnKF assimilation will be discussed in this paper. It poses a challenge to EnKF assimilation in resolving the high-value measurements in this region.

The performance of EnKF deteriorates when position errors are present. The underlying mechanism can be best understood by examining Fig. 2(a). At time point  $t_0$ , there are ensemble model simulations (gray dashed lines) distributed across the three-dimensional space. The black line and blue star represent the average of model ~~ensembles~~ensemble and observations, 400 respectively. As clearly depicted, there is a positional mismatch between the ensemble model simulations and observations. Following the assimilation analysis, the intensity of the dust plume is adjusted to better match the observations. However, in the spatial domain outside the priori, the dust concentration is reduced to near-zero levels. The observations in this area, containing valuable information about dust load, contribute little to correcting the dust load. This is due to the unanimous agreement on the dust load from the model ~~ensembles~~ensemble, which represents low uncertainty. In such cases, the assimilation analysis favors 405 the model results and disregards the observations. Consequently, the a posteriori estimate is biased as a result of ~~imbalanced~~  
~~uncertainties~~ensemble underdispersion.

### 3.2 VTS-EnKF

To efficiently perform the assimilation analysis with both the intensity and position errors present, we apply a "valid time shifting" method into the EnKF. The strategy is illustrated in Fig. 2(b). Instead of using the ensemble simulations solely at 410 the exact assimilation analysis instant  $t_0$ , as shown in panel a, ~~ensembles~~ensemble members at neighboring moments are also introduced to expand the ensemble group. These resampled ~~ensembles~~ensemble members at neighboring times represent the potential positions of the actual dust plume. The enlarged ~~ensembles~~ensemble exhibit a more extensive spread of the dust plume in the spatial domain compared to those displayed in panel a. The joint ensemble model simulations then capture uncertainty in both intensity and position. The a posteriori estimate (red line) is adjusted to better fit the observations, with 415 both of these errors resolved.

Mathematically, the EnKF with VTS procedures are very similar to those of EnKF, except that the original  $\mathbf{X}^f$  is replaced by  $\mathbf{X}^{f,new}$ , which stores the enlarged ensemble members at the assimilation analysis instant and neighboring times. It starts with

$$\mathbf{X}^{f,new} = [\mathbf{x}_{t-\tau}^{f,1}, \mathbf{x}_{t-\tau}^{f,2}, \dots, \mathbf{x}_{t-\tau}^{f,N}, \mathbf{x}_t^{f,1}, \mathbf{x}_t^{f,2}, \dots, \mathbf{x}_t^{f,N}, \mathbf{x}_{t+\tau}^{f,1}, \mathbf{x}_{t+\tau}^{f,2}, \dots, \mathbf{x}_{t+\tau}^{f,N}] \quad (9)$$

420 Let  $t$  be the exact assimilation time, and  $\tau$  be the time interval. Then  $t - \tau$  represents the time in the past, and  $t + \tau$  represents the time in the future. It is noteworthy that the time axis, denoted by  $t - \tau$  and  $t + \tau$ , is utilized solely to illustrate the application of ensemble simulations at different time direction in the formula. However, in practical applications, ensembles-ensemble members from multiple adjacent time instants can be incorporated, as demonstrated in the horizon choice utilized in this study (as presented in Table 1).

425 Subsequently, the ensemble-based background covariance  $\mathbf{P}^f$ , Kalman gain  $\mathbf{K}$  and posteriori state  $\mathbf{x}^a$  will be updated with the  $\mathbf{X}^{f,new}$  in Eq. 6 ~ 8, respectively.

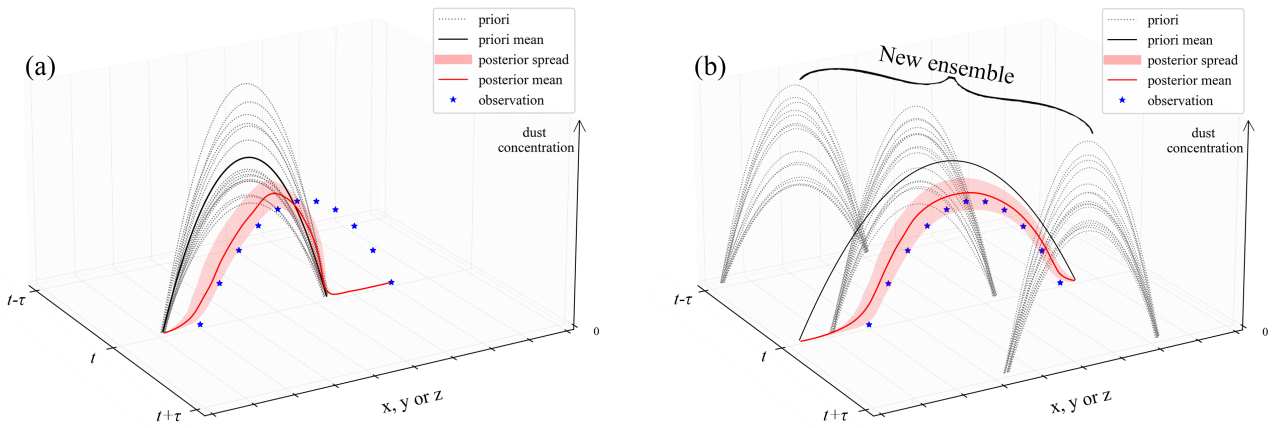


**Figure 2.** Strategy illustration of ensemble Kalman filter (EnKF) (a) and ensemble Kalman filter with VTS (VTS-EnKF) (b). Figure axis left represents the time and right represents the position of the dust field in 3D space. The vertical axis represents the intensity of the dust.

The localization method is also adopted here to cut off the spurious correlation in  $\mathbf{P}^f$  and constrain the background covariance to a certain distance. The localization matrix is constructed following Gaspari and Cohn (1999) (Eq. A.27) with a distance threshold  $L_{thres}$ . The details about the construction of  $\mathbf{L}$  can be found in Supporting Information. The localized  $\mathbf{P}^{f,local}$  is 430 obtained by point to point multiply with localization matrix  $\mathbf{L}$ .

$$\mathbf{P}^{f,local} = \mathbf{P}^f \circ \mathbf{L} \quad (10)$$

With the localized  $\mathbf{P}^{f,local}$ , the localized posteriori estimation  $\mathbf{x}_t^{a,i}$  can be updated via Eq. 7 and Eq. 8.

Both the EnKF and EnKF with VTS described above are embeded into our self-designed assimilation toolbox, PyFilter (Pang, last access: May. 2024). This toolbox features a flexible interface for linking to numerical models (Pang et al., 2023), 435 such as the dust storm forecasting model LOTOS-EUROS used in this study.

### 3.3 Experiment descriptions

DSE1 and DSE2 are chosen as the cases for the test. The BC-PM<sub>10</sub> observations are assimilated. The first assimilation analysis did not commence until the dust plume was detected by the ground-based observation network and a position mismatch emerged. An identification index is also designed to objectively discriminate the position error as can be found in Eq. S3

440 S6 in Supplementary. Three sequential EnKF analyses are conducted in each dust event at three-hour intervals. The timeline for DSE1 and DSE2 is depicted in Fig. 3.

Taking DSE1 as an example, the initial assimilation analysis is performed at 11:00 March 15, when an apparent position error was present, as illustrated in Fig. 1 (a.2). The last analysis is carried out at 17:00 March 15. As the dust loading decreases rapidly when the plume moves further southeast, no additional assimilation is performed. A rolling forecast (red line with 445 arrow) is generated based on the optimized dust concentration field with a 24-hour horizon for the purpose of examining forecast skill.

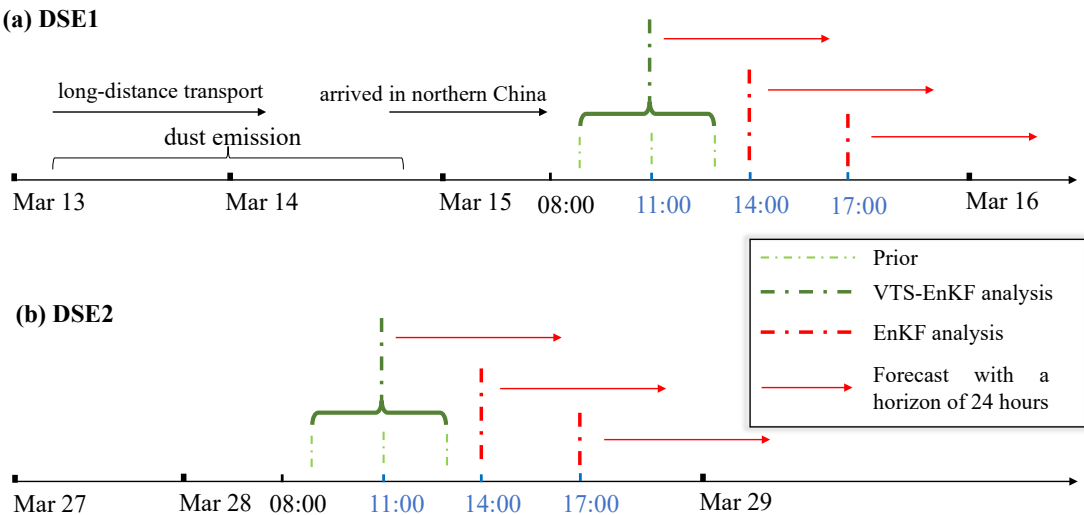


**Figure 3.** Sequential assimilation time set for DSE1 (a) and DSE2 (b). Take DSE1 for instance, the assimilation analysis is performed at the intervals of 3 hours from 11:00 to 17:00 and the rolling forecast is made with a horizon of 24 hours based on the assimilation analysis. The EnKF with VTS and EnKF is performed in turn.

To evaluate the performance of the VTS-EnKF-implemented dust storm forecasting system, data assimilation experiments are conducted on two spring dust events in 2021. Experiment settings are shown in Table 1. *Control* represents the ensem-

ble model forecast throughout the entire dust storm period. *EnKF* and *L500* denote the assimilation-based forecasts by  
450 EnKF and localized EnKF (LEnKF) with a localization distance threshold of 500 km, respectively. *VTS-EnKF* and *VTS-L500*  
represent the assimilation-based forecasts by VTS-EnKF and VTS-EnKF with a localization distance threshold of 500 km.  
Note that various distance thresholds have been tested for localization, and a choice of 500 km is found to provide the optimal  
assimilation analysis and forecast in our tested cases. The metrics, Root Mean Square Error (RMSE) and Normalized Mean  
Bias (NMB), are employed in this paper to evaluate system performance. Calculation of the metrics is mentioned in supporting  
455 information.

In EnKF-based experiments, *EnKF* and *L500*, the ensemble number N is set to 32, which is found to be sufficient to  
represent the uncertainty in the dust simulation while remaining computationally affordable. Testing with N greater than 32  
shows only limited improvements. For VTS-EnKF experiments, the ~~ensembles are ensemble is~~ expanded as they incorporate  
460 ~~ensemble~~-simulations from neighboring instants. To cover the potential positions of the dust plume, neighboring times with  
 $\pm 1$  and  $\pm 2$  hours apart are empirically chosen in this paper. As demonstrated in Table 1, the ensemble number is extended  
to 160 when EnKF with VTS is applied, and the neighboring time stamps of 9:00, 10:00, 12:00, and 13:00 are selected. The  
160 ensemble dust simulations are updated according to the EnKF principles and forwarded synchronously for the new rolling  
forecast; they will serve as the prior in the subsequent assimilation analysis.

Experiments for the VTS-EnKF with equal ~~ensembles ensemble members~~ to EnKF are designed, as referred to *VTS-EnKF*-  
465 *small* and *VTS-L500-small*. They ~~starts start~~ with central 8 ~~ensembles ensemble members~~ and are extended to 32 ~~ensembles~~  
by incorporating neighboring  $\pm 1$  and  $\pm 2$  hours with  $4 \times 6$  ~~ensembles ensemble members~~. Furthermore, to test the sensitivity of  
neighboring time interval, VTS-EnKF experiments with different intervals are also designed. Time intervals ranging from 1 to  
5 hours are selected to test the impact, which are referred to as *VTS-EnKF-t1*, *VTS-EnKF-t2*, *VTS-EnKF-t3*, *VTS-EnKF-t4* and  
*VTS-EnKF-t5*.

## 470 4 Results and discussions

The results are discussed in the aspects of assimilation analysis and model forecast. The benefits of using our EnKF with VTS  
algorithm for the dust storm simulation with position errors are emphasized.

### 4.1 Impact on assimilation analysis

Figure 4 displays the spatial distribution of ground BR-PM<sub>10</sub> observations (scatter) and dust field forecasts from the average of  
475 the ~~ensembles ensemble~~ (panel a.1), the posteriori from EnKF analysis (panel a.2) and EnKF with localization (panel a.3), the  
average of the enlarged ~~ensembles ensemble~~ (panel b.1), the posteriori from VTS-EnKF analysis (panel b.2) and VTS-EnKF  
analysis with localization (panel b.3) at 11:00, 15th March, 2021 China Standard Time (CST). It should be noted that the aver-  
age dust concentrations in panel b.1 are calculated from the 160 ensemble simulations used in VTS-EnKF, which slightly differ  
from the average of 32 ~~ensembles ensemble members~~. In DSE1, the RMSE and NMB from the pure ensemble model simula-  
480 tion are as high as 856.36  $\mu\text{g m}^{-3}$  and -78.31 %. Both EnKF and LEnKF assimilation analyses achieve very limited

**Table 1.** Experiment settings.

Name	Ensemble size used by analysis and forecast	Initial assimilation time set (hour)	Ensemble set	Localization distance (km)
<i>Control</i>	32	None	[32]	None
<i>EnKFBasic</i>	32	$t$	[32]	None
<i>L500</i>	32	$t$	[32]	500
<i>VTS-EnKF</i>	160	$t-2, t-1, t, t+1, t+2$	[32,32,32,32,32]	None
<i>VTS-L500</i>	160	$t-2, t-1, t, t+1, t+2$	[32,32,32,32,32]	500
<i>VTS-EnKF-small</i>	32	$t-2, t-1, t, t+1, t+2$	[6,6,8,6,6]	None
<i>VTS-L500-small</i>	32	$t-2, t-1, t, t+1, t+2$	[6,6,8,6,6]	500
<i>VTS-EnKF-t1</i>	96	$t-1, t, t+1$	[32,32,32]	None
<i>VTS-EnKF-t2</i>	96	$t-2, t, t+2$	[32,32,32]	None
<i>VTS-EnKF-t3</i>	96	$t-3, t, t+3$	[32,32,32]	None
<i>VTS-EnKF-t4</i>	96	$t-4, t, t+4$	[32,32,32]	None
<i>VTS-EnKF-t5</i>	96	$t-5, t, t+5$	[32,32,32]	None
<i>VTS-EnKF-t6</i>	96	$t-6, t, t+6$	[32,32,32]	None

improvement in estimating the dust state field. As shown in panel a.2 and panel a.3, the RMSE and NMB remain high at 819.04  $\mu\text{g m}^{-3}$  and -75.65 % in *EnKFBasic*, and 782.57  $\mu\text{g m}^{-3}$  and -73.52 % in *L500*. The main reason for this is the ~~imbalance uncertainty between the ensemble simulations and the observations~~ ~~ensemble underdispersion~~, as described in Sect. 3.2. As observed in the light blue box in panel a.1, the simulated dust plume is located farther southeast compared to the

485 PM<sub>10</sub> measurements. This snapshot exhibits an apparent position error. After EnKF analysis, the simulated dust plume in the light blue box barely changes, as depicted in panel a.2. Numerous ground stations in this area report high PM<sub>10</sub> concentrations, but the assimilated dust field fails to resolve most of them. The localization method offers limited assistance in this situation, as illustrated in panel a.3. With the unresolved positional error, the EnKF, which focuses more on intensity correction, is much less effective.

490 When it comes to the VTS-EnKF analysis result, an improved dust field can be noticed. Concerning the Root Mean Square Error (RMSE) and Normalized Mean Bias (NMB), the two priors depicted in panels a.1 and b.1 exhibit highly similar performances. However, slight differences do exist. For instance, the average of the expanded 160-member ensemble used in VTS-EnKF displays a marginally broader spread. The increased ensemble size provides more room for representing background uncertainties. The enhanced capacity for this is best illustrated in Fig. 6 (a), which exhibits the uncertainty quantified 495 by the enlarged ensemble simulations in VTS-EnKF formulations. ~~High uncertainty values are seen in pixels where large model minus observation errors are present, such as within the light blue box. This allows the posterior to be adjusted in order to better conform to the observations~~ ~~This expansion of the uncertainty spread effectively addresses the issue of ensemble underdispersion, thereby boosting the EnKF's capability to handle position errors~~. In contrast, the relatively low uncertainty

over these areas depicted in Fig. 1 (b.2) suggests that the EnKF method is highly confident in the absence of aerosols and does 500 not require any modification. The observations are effectively assimilated in the VTS-EnKF analysis. As displayed in panel b.2, the dust plume within the light blue box is adjusted to better match the observations. In particular, the dust to the east of the marked region is well represented in comparison to the posteriori of *EnKFBasic*. The RMSE and NMB are reduced to 742.33  $\mu\text{g m}^{-3}$  and -68.21 %. Moreover, the posteriori of *VTS-L500* yields an improved dust field with the RMSE and NMB further reduced to 696.1  $\mu\text{g m}^{-3}$  and -63.93 %. The implementation of the localization method eliminates 505 spurious correlations and generates a background error covariance that more accurately describes the model uncertainties. Despite the noticeable improvements achieved in DSE1, the residual errors, as indicated by the RMSE and NMB metrics, remain relatively high. This is mainly due to some observations with extremely high value (exceeding 5000  $\mu\text{g m}^{-3}$ ), which is far higher than the surrounding stations and hard for the EnKF to adapt. In particular, the western extent of the dust plume is covered by the insufficient stations, which results in an inadequate representation of the dust load. By incorporating neighboring 510 ~~ensembles~~ensemble, the dust plume is extended wilder, ~~as can't be verified by the observations~~. In the future research, assimilating satellite-derived dust optical depth (DOD) observations that have broader coverage may help to better constrain the enlarged ensemble.

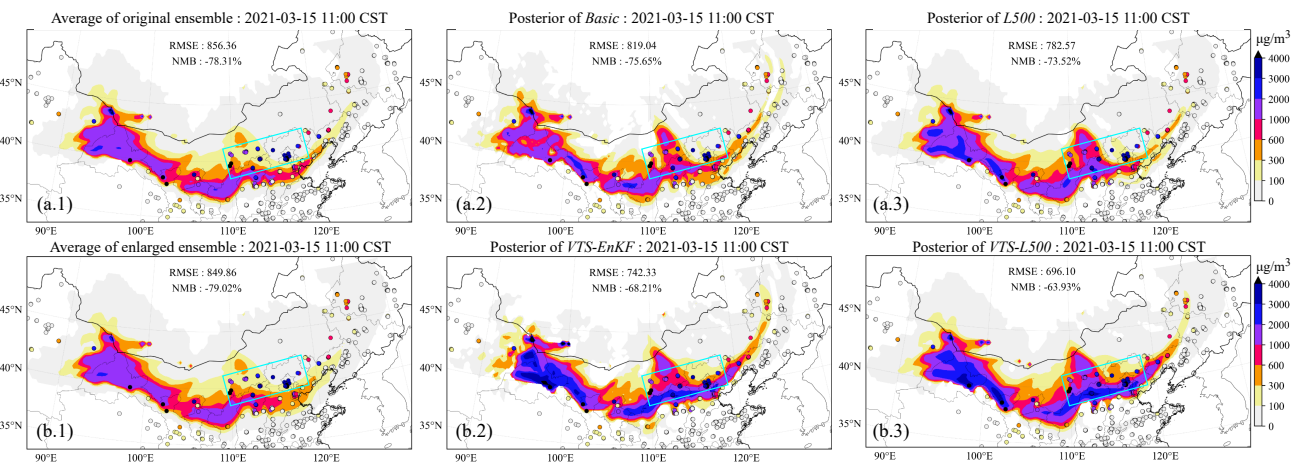


**Figure 4.** Spatial distribution of ~~ground-based BR-PM<sub>10</sub> observations (scatter) and~~ simulated dust plume (SDP) on surface from average of ensemble members at central time ensemble model mean (a.1), the posteriori SDP updated by EnKF (a.2), the posteriori SDP updated by EnKF with localization (a.3), central and neighboring time ensemble model mean (b.1), the posteriori SDP updated by VTS-EnKF (b.2), the posteriori SDP updated by VTS-EnKF with localization (b.3) at 11:00, 15th March 2021 (CST). The filled circles are ground-based BR-PM<sub>10</sub> observations. CST: China Standard Time.

Figure 5 presents the spatial distribution of ground-based BR-PM<sub>10</sub> observations (scatter) and dust concentration forecasts from the average of model ~~ensembles ensemble~~ (panel a.1), EnKF (panel a.2), and LEnKF analysis (panel a.3), as well as 515 the average of the enlarged model ~~ensembles ensemble~~ (panel b.1), VTS-EnKF (panel b.2), and VTS-EnKF with localization analysis (panel b.3) at 11:00, March 28th, 2021 CST. During this assimilation snapshot in DSE2, the model-simulated dust

field is observed to have moved further southeast, as depicted in panel a.1. As illustrated by the light blue box in panel a.1, the model-simulated dust plume missed most of the observations with high  $PM_{10}$  concentrations. Consequently, although the EnKF analysis remains effective in this case, dust in light blue box is nearly unchanged. The RMSE and NMB are reduced to 520 348.13  $\mu g m^{-3}$  and -45.96 % in the *EnKFBasic* scenario, with further reductions to 301.38  $\mu g m^{-3}$  and -39.12 % when the localization method is employed in the *L500* case.

For the enlarged *ensemblesensemble*, the RMSE and NMB of the priori for *VTS-EnKF* are 433.08  $\mu g m^{-3}$  and -8.93 %. With *VTS-EnKF* assimilation, the RMSE of the posterior further decreases to 246.23  $\mu g m^{-3}$ , and the NMB is -31.61 % in *VTS-EnKF*. Unlike the *EnKFBasic*, the dust plume in light blue box is noticeably *tunedoptimized* to better fit the 525 observations. *These error and bias values*, *RMSE and NMB* are significantly lower than those obtained with the *EnKFBasic*, thanks to the better-scaled background covariance displayed in Fig. 6. Moreover, by incorporating localization, the RMSE and NMB are further reduced to 221.15  $\mu g m^{-3}$  and -27.23 % in *VTS-L500*. The dust load within the light blue box (panel b.3) is accurately reproduced within its actual range (2000~3000  $\mu g m^{-3}$ ).

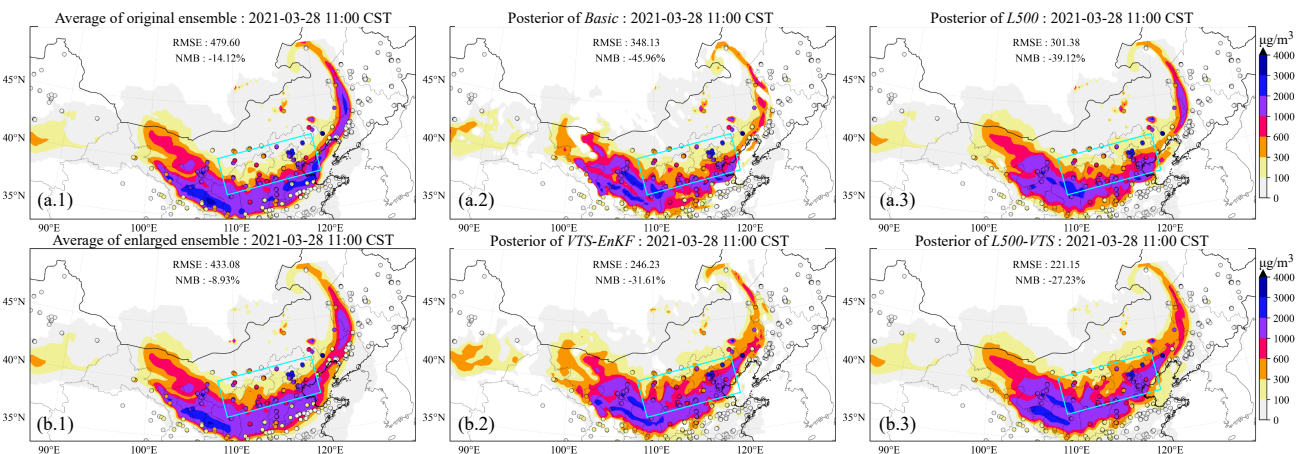


**Figure 5.** Spatial distribution of *ground-based BR-PM<sub>10</sub> observations (scatter)* and *simulated dust plume (SDP)* on surface from *average of ensemble members at central time ensemble model mean* (a.1), the *posterior SDP updated by EnKF* (a.2), the *posterior SDP updated by EnKF with localization* (a.3), *central and neighboring time ensemble model mean* (b.1), the *posterior SDP updated by VTS-EnKF* (b.2), the *posterior SDP updated by VTS-EnKF with localization* (b.3) at 11:00, 28th March 2021 (CST). *The filled circles are ground-based BR-PM<sub>10</sub> observations. CST: China Standard Time.*

## 4.2 Impact on forecast skills

530 In addition to the snapshots of the assimilation analysis, an comprehensive evaluation of forecast skills is also necessary to see the performance of *VTS-EnKF* algorithm. A general evaluation on the forecasting skills is carried out in this section.

Figure 7 presents the time series of RMSE and NMB for the 24-hour dust forecast after three assimilation analyses in DSE1 (starting from 11:00, 14:00, and 17:00). In these cases, the *Control run* generates a dust field with a high RMSE (ranging

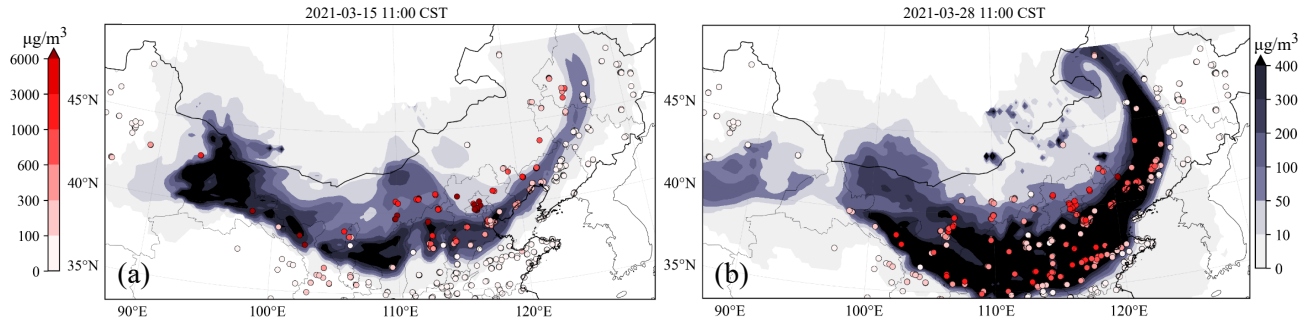


**Figure 6.** Spatial distribution of standard deviation from [model ensembles with scatter of model-minus-observation differences \(absolute value\) ensemble members](#) at 11:00 in DSE1(a) and 08:00 in DSE2(b). The initial assimilation analysis is performed at these time. [The filled circles are model-minus-observation differences \(absolute value\)](#). Colorbar left is for model-minus-observation differences and right is for standard deviation. [CST: China Standard Time](#).

from over 800  $\mu\text{g m}^{-3}$  to around 600  $\mu\text{g m}^{-3}$  and a large NMB (consistently around -85 %). The EnKF analysis, however, does not improve this dust forecast after the initial assimilation. In fact, the RMSE and NMB of the dust forecast from the [EnKFBasic](#) scenario are nearly identical to the *Control run*, as evidenced by the comparison between the black dashed line and the blue line in panel a. This result can be primarily attributed to the position error discussed in Sect. 2.4. The EnKF algorithm offers minimal assistance in correcting the model simulation when position errors are present. These errors are not occasional but cumulative, as demonstrated in the subsequent two assimilation timestamps at 14:00 and 17:00, during which the assimilation analysis shows limited improvement over the situation. Moreover, it has been observed that the localization method [is unable to enhance the forecast only improves the forecast slightly](#) in the presence of position errors. Similar for NMB, as depicted in panel b, the improvements are also insignificant. The NMB for the *Control*, [EnKFBasic](#), and *L500* scenarios remains consistently around -85 % throughout the entire forecast time range.

By applying the VTS-EnKF analysis, a reduction of RMSE [is compared to the model run and EnKF can be](#) observed in panel a. There is an approximate decrease of 100  $\mu\text{g m}^{-3}$  in VTS-EnKF compared to [EnKFBasic](#), which indicates that the VTS-EnKF analysis effectively corrects the position error. At the subsequent assimilation timestamps, this situation improves, with an even greater decrease in RMSE. The RMSE of *VTS-L500* is slightly lower than that of *VTS-EnKF*. As for NMB, quite promising results are achieved. In *VTS-EnKF*, the NMB decreases stepwise at three time points, from around -75 % at 11:00 to around -70 % at 14:00, and finally to around -65 %. The VTS-EnKF algorithm gradually takes effect over the three assimilation analyses. In *VTS-L500*, the localization method demonstrates its efficacy, especially after the third assimilation timestamp at 17:00. The NMB is reduced to around -60 %, which is significantly lower than that of the *L500*.

Figure 8 displays the time series of RMSE and NMB on a 24-hour dust forecast after three assimilation analyses in DSE2. Unlike DSE1, [EnKFBasic](#) in DSE2 does improve the dust forecast in terms of RMSE and NMB. The RMSE drops from around 500  $\mu\text{g m}^{-3}$  to less than 400  $\mu\text{g m}^{-3}$  at the initial assimilation timestamp (11:00). NMB here is higher

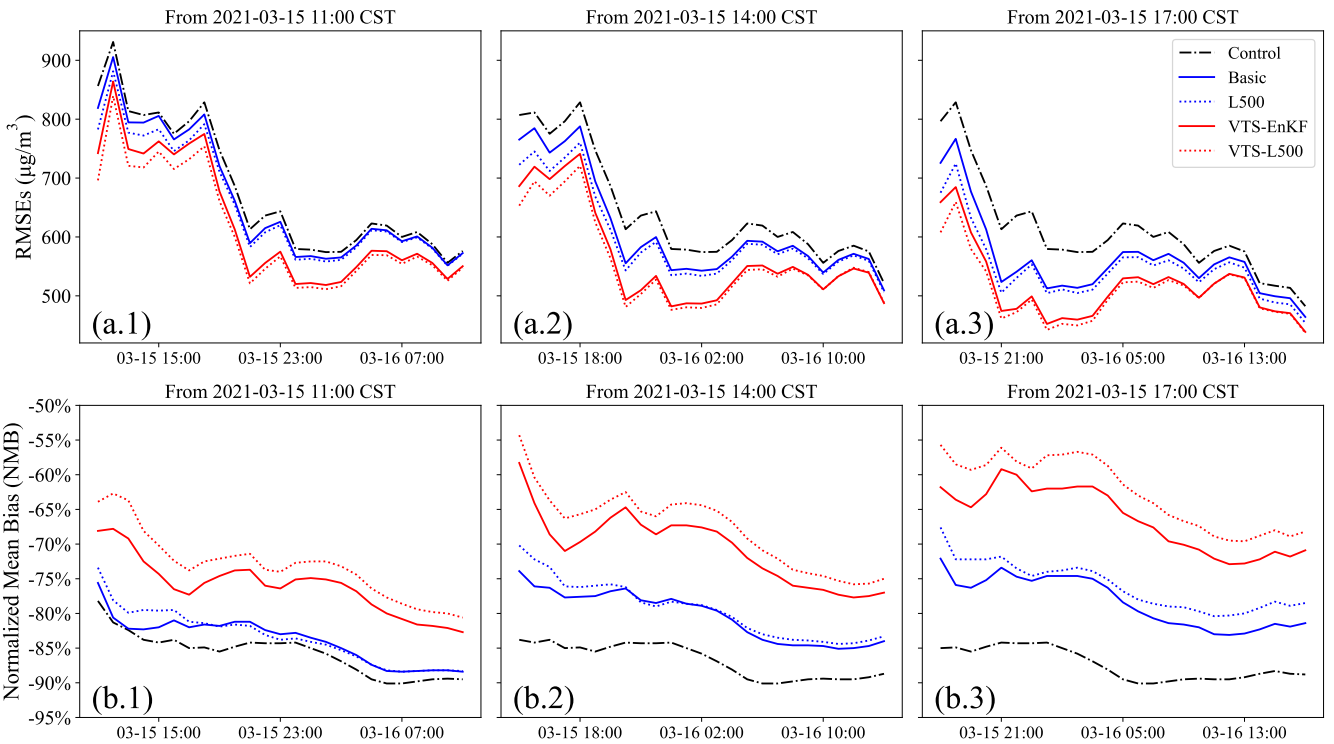


**Figure 7.** Time series of 24-hour Root Mean Square Error (RMSE) on the dust forecast starting from 11:00 (a.1), 14:00 (a.2), 17:00 (a.3) and normalized mean bias (NMB) starting from 11:00 (b.1), 14:00 (b.2), 17:00 (b.3) on 15th March 2021. [CST: China Standard Time](#).

555 than *Control* due to the complementary effect of NMB. The overestimation is corrected while the underestimation caused by position error is not corrected. No further reduction is observed at subsequent time points. As can be seen in panels a.2 and a.3, the RMSE of *EnKFBasic* remains almost constant compared to panel a.1. This indicates that the position error is not corrected, and it constitutes part of the RMSE that is difficult to eliminate. The trend of NMB also reflects this situation. *L500* is unable to correct the position error, although it does help reduce the error to some extent.

560 In the scenario of the VTS-EnKF analysis, an improvement in the dust forecast of DSE2 is obtained. A general reduction of RMSE (around 50  $\mu\text{g m}^{-3}$ ) in *VTS-EnKF* compared to *EnKFBasic* can be seen in panel a.1. Furthermore, in the subsequent forecasts, a steady decrease in RMSE is noted. The RMSE fluctuates around 250  $\mu\text{g m}^{-3}$  after 14:00 and 200  $\mu\text{g m}^{-3}$  after 17:00. *VTS-L500* exhibits a similar pattern to *VTS-EnKF* for most of the forecast. Considering the NMB, as shown in panel b, the NMB of *VTS-L500* demonstrates trivial superiority over *VTS-EnKF*. In DSE2, the *EnKFBasic* and *L500* have already achieved well-reproduced dust fields, while the *VTS-EnKF* and *VTS-L500* can further improve these fields by correcting the position error.

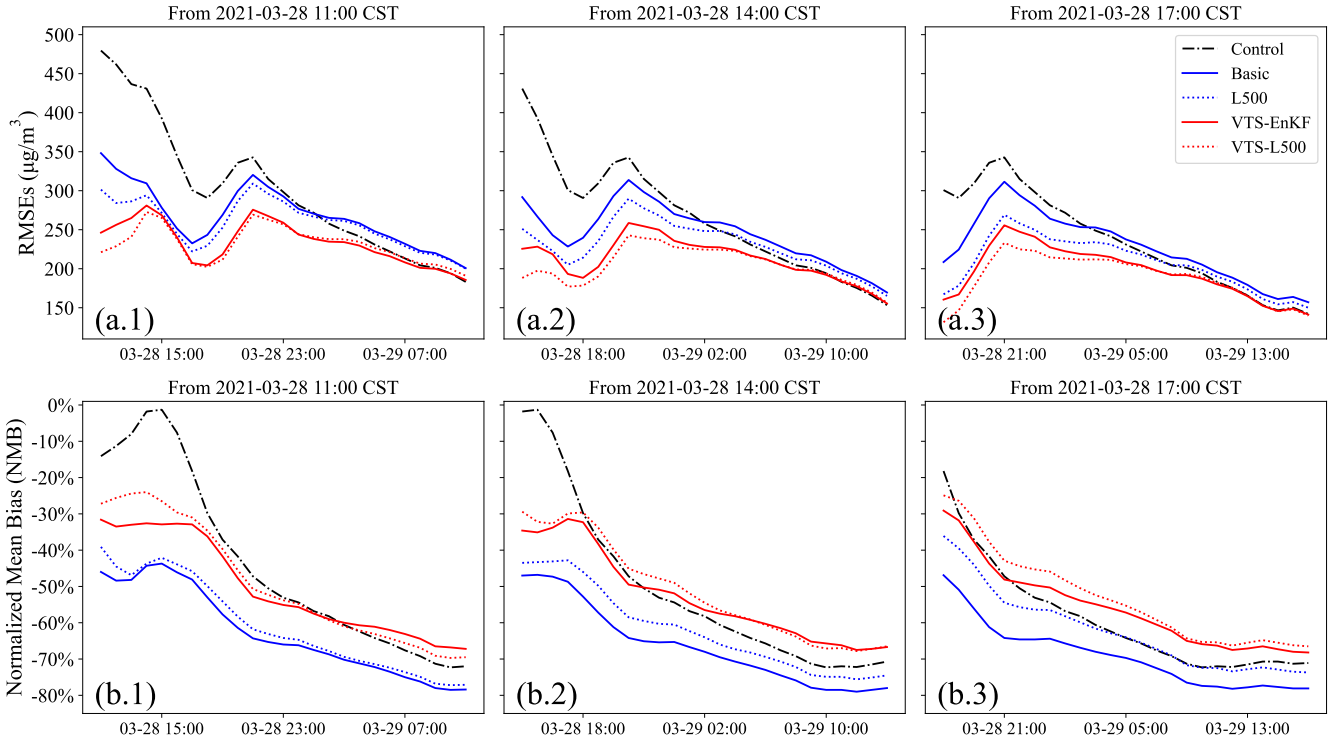


**Figure 8.** Time series of 24-hour Root Mean Square Error (RMSE) on the dust forecast starting from 08:00 (a.1), 11:00 (a.2), 14:00 (a.3) and normalized mean bias (NMB) starting from 08:00 (b.1), 11:00 (b.2), 15:00 (b.3) on 28th March 2021. [CST: China Standard Time](#).

#### 4.3 Assessment of ~~smaller ensembles~~<sup>fewer ensemble members</sup>

To further assess the performance of VTS-EnKF, VTS-EnKF experiments with same ~~ensembles~~<sup>ensemble members</sup> as the EnKF are designed. They are referred to as *VTS-EnKF-small* and *VTS-L500-small*, respectively. The total 32 ~~ensembles~~<sup>ensemble members</sup> 570 are composed of 8 central ~~ensembles~~<sup>ensemble members</sup> and 4×6 ~~ensembles~~<sup>ensemble members</sup> from neighboring  $\pm 1$  and  $\pm 2$  hours. Figure 9 displays the time series of RMSE and NMB on a 24-hour dust forecast after three assimilation analyses in DSE1. In terms of RMSE, *VTS-EnKF-small* only shows slightly better performance than the EnKF. This mostly caused by the sampling error arises from limited ~~ensembles~~<sup>ensemble members</sup> resampled from the central ~~ensembles~~<sup>ensemble members</sup> 575 (only 8 ~~ensembles~~<sup>ensemble members</sup>). However, by applying the localization, the RMSE is noticeably reduced by 100  $\mu\text{g m}^{-3}$ . The performance is comparable to the *VTS-L500* (red dash line) with totally 160 ~~ensembles~~<sup>ensemble members</sup>. By mitigating the sampling error, the VTS-EnKF's capability of handling the position error can be revealed, which can be noticed by comparison with *L500* and *VTS-L500-small*. This improvement can be better seen in NMB. NMB of *VTS-L500-small* is much lower than the *EnKF Basic* and *L500*. Its performance is also comparable to the *VTS-L500* with 160 ~~ensembles~~<sup>ensemble members</sup>.

580 Same experiments on DSE2 are also carried out. Results can be found in Fig. S2 in supporting information. Similar to DSE1, the *VTS-EnKF-small* achieves slightly better RMSE and NMB than *EnKFBasic* and *L500*. While in *VTS-L500-small*, noticeable improvements can be found especially for the forecast after the second and last assimilation. Reduction of 100  $\mu\text{g m}^{-3}$  in RMSE and 20% in NMB are obtained.

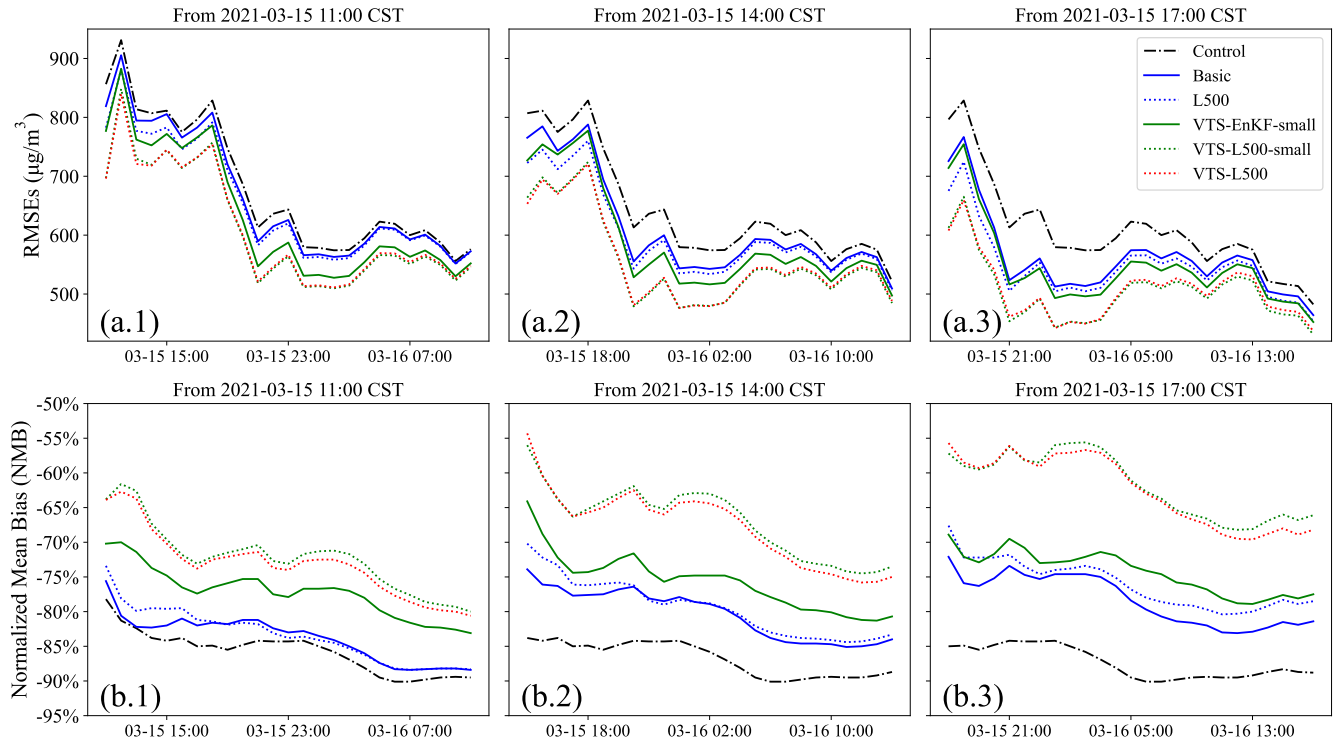


**Figure 9.** Time series of 24-hour Root Mean Square Error (RMSE) on the dust forecast starting from 11:00 (a.1), 14:00 (a.2), 17:00 (a.3) and normalized mean bias (NMB) starting from 11:00 (b.1), 14:00 (b.2), 17:00 (b.3) on 15th March 2021. [CST: China Standard Time](#).

#### 4.4 Sensitivity of time interval

585 Previous researches have found that an improper neighboring time interval  $\tau$  can lead to undesirable results, such as less-effective ensemble members (interval too small) ( $\tau$  too small) or ensemble member clustering and unrepresentative ensemble covariances ( $\tau$  too large) (Xu et al., 2008; Gasperoni et al., 2022, 2023). To explore the sensitivity of the choice of neighboring time interval, series of VTS-EnKF experiments with different neighboring time interval were carried out. Time intervals ranging from 1 to 6 hour were tested. As shown in Fig. 10, snapshots from 6 experiments on DSE1 clearly depicts the trend. In general, 590 all the VTS-EnKF experiments show better performance than EnKF. While in terms of specific time interval, different patterns can be noticed. For short intervals including 1 and 2 hour, there is not sufficient ensemble spread to account for the position error. Thus there are still position error remaining and RMSE is still high. For long intervals including 5 and 6 hour, dust plume

is clustered away from central dust plume. Three dust branches are noticed in *VTS-EnKF-t5* and an overly backwards dust plume is noticed in *VTS-EnKF-t6*. In this case, 3-hour interval is the best choice with the lowest RMSE (696.11  $\mu\text{g m}^{-3}$ ) and NMB (-63.5 %).

595 Same experiments on DSE2 are also performed and snapshots are shown in Fig. S3. Similar patterns are found on DSE2. Lowest RMSE and NMB are achieved in *VTS-EnKF-t4*. Too short interval leads to inability in position error correction and too long interval leads to excessive dust plume. Considering both cases, 3-hour interval is the preferred choice which holds the capability to handle position and not creates excessive clustered dust plume.

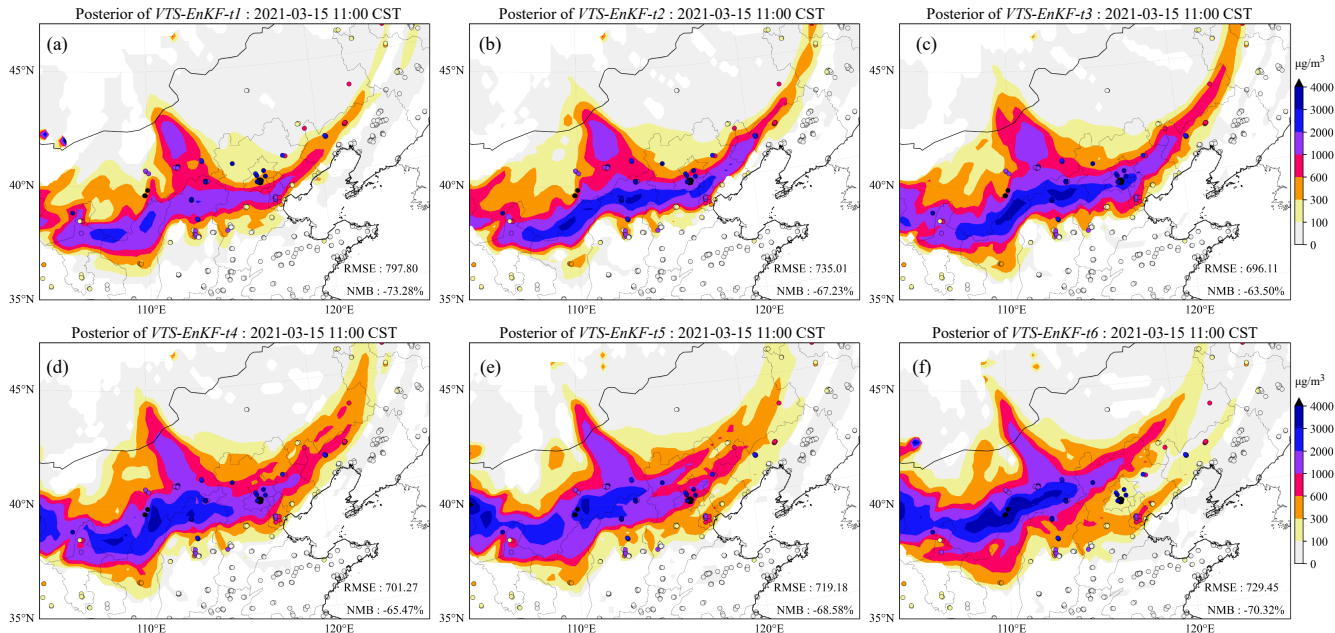


**Figure 10.** Spatial distribution of ground-based BR-PM<sub>10</sub> observations (scatter) and simulated dust plume (SDP) on surface from the posteriori SDP updated by *VTS-EnKF-t1* (a), the posteriori SDP updated by *VTS-EnKF-t2* (b), the posteriori SDP updated by *VTS-EnKF-t3* (c), the posteriori SDP updated by *VTS-EnKF-t4* (d), the posteriori SDP updated by *VTS-EnKF-t5* (e), the posteriori SDP updated by *VTS-EnKF-t6* (f) at 11:00, 15th March 2021 (CST).

## 600 5 Conclusions

The Chemistry Transport Model (CTM) is a powerful tool for air pollutant forecasting. However, as a simplified version of the real atmospheric world, it suffers from various deficiencies, particularly in two major uncertainties: emissions and meteorology. Uncertainty from meteorological fields can cause model forecast errors, especially in long-distance transport. In 605 dust storm forecasting applications, a position error is noted that significantly degrades the overall performance of the forecast and prevents the EnKF assimilation algorithm from effectively incorporating observational data.

The background error covariance of EnKF is generally designed to represent the intensity and position uncertainty. However, when the position error is sufficiently large, the background error covariance can't adequately represent the position error, which is highly non-Gaussian. In the case of the long-distance dust storm tracking, the EnKF is incapable of thoroughly resolving the observations. Observations over low model uncertainty pixels are 'ignored' by the EnKF algorithm. To address this issue, 610 a valid time shifting method is coupled with EnKF. This VTS-EnKF methodology introduces uncertainty of the dust plume position into the background error covariance by incorporating extra ensemble simulations at neighboring time instances. This enlarged ensemble not only reflects the uncertainty of dust intensity but also reveals the potential positions of the plume, allowing for more accurate and effective assimilation and improving dust storm forecasting.

The VTS-EnKF algorithm was tested on two super dust storm events (DSE1 and DSE2) that occurred in Spring 2021. 615 Several experiments were designed to examine the performance of the VTS-EnKF algorithm in these cases, with a focus on differences between EnKF and VTS-EnKF. In terms of assimilation analysis, the VTS-EnKF analysis corrected the position error in DSE1 to a large extent. Comparison between the standard deviations from posterior of EnKF and VTS-EnKF explained for it. The standard deviations from VTS-EnKF analysis indicated wilder potential dust spread and were more consistent with the model-minus-observation. Observations that were 'ignored' by EnKF were comprehensively resolved in VTS-EnKF, 620 resulting in decreased RMSE and NMB. For DSE2, the position error was not as significant as in DSE1; however, imbalanced uncertainties ensemble underdispersion were also observed. Nevertheless, VTS-EnKF still produced an improved dust field with lower RMSE and NMB compared to EnKF. In both cases, the localization method helped reduce RMSE and NMB. Regarding the forecast performance, promising results were obtained. In DSE1, the RMSE and NMB revealed that EnKF provides limited improvements compared to model run. In contrast, VTS-EnKF provided a dust field forecast with reduced 625 errors, especially in terms of NMB. Additionally, the localization method contributed to further reducing the error. Overall, the VTS-EnKF algorithm demonstrated improved performance in assimilation analysis and forecasting for the tested dust storm events compared to the traditional EnKF approach.

Assessment of equal ensembles ensemble members between EnKF and VTS-EnKF is carried out. VTS-EnKF with smaller 630 ensembles ensemble size shows slightly improved metrics than EnKF. While by applying localization, more reduction in RMSE and NMB can be noticed and its performance is comparable to the VTS-EnKF with larger ensembles ensemble size. This is due to the corrected sampling error within limited ensembles ensemble members. Comparison between them confirms VTS-EnKF's ability in handling position error. Sensitivity of neighboring time interval choice is also examined. Too short interval leads to inability in position error correction and too long interval leads to excessive dust plume. Considering both cases, 3-hour interval is the preferred choice.

635 *Code and data availability.* The EnKF with VTS code is archived on Zenodo at <https://doi.org/10.5281/zenodo.7611976> (Pang, last access: May. 2024). The PM<sub>10</sub> data used in this study is also archived on Zenodo at <https://doi.org/10.5281/zenodo.6459866> (Jin, 2022). The real-time PM<sub>10</sub> data established by the Ministry of Ecology and Environment is available to the public at <https://quotsoft.net/air> (Wang, last

access: May. 2024). The source code and user guide of the LOTOS-EUROS model could be obtained from <https://lotos-euros.tno.nl> (TNO, last access: May 2024).

640 *Author contributions.* JJ conceived the study and designed VTS-EnKF algorithm. MP wrote the code of the assimilation and carried out the experiments and evaluation. AS, HJ, WH, BB, JX, LF, JL, HXL and HL provided useful comments on the paper. MP and JJ prepared the manuscript with contributions from HJ and all others co-authors.

*Acknowledgements.* This work is supported by the National Natural Science Foundation of China [grant No. 42105109 and 42205031] and Natural Science Foundation of Jiangsu Province (No. BK20210664).

645 **Competing interests**

The authors declare that they have no conflict of interest.

## References

Amezcua, J. and Van Leeuwen, P. J.: Gaussian Anamorphosis in the Analysis Step of the EnKF: A Joint State-Variable/Observation Approach, *TELLUS A*, 66, 23493, <https://doi.org/10.3402/tellusa.v66.23493>, 2014.

650 An, L., Che, H., Xue, M., Zhang, T., Wang, H., Wang, Y., Zhou, C., Zhao, H., Gui, K., Zheng, Y., Sun, T., Liang, Y., Sun, E., Zhang, H., and Zhang, X.: Temporal and Spatial Variations in Sand and Dust Storm Events in East Asia from 2007 to 2016: Relationships with Surface Conditions and Climate Change, *Sci. Total Environ.*, 633, 452–462, <https://doi.org/10.1016/j.scitotenv.2018.03.068>, 2018.

Bannister, R. N.: A Review of Operational Methods of Variational and Ensemble-Variational Data Assimilation, *Q. J. R. Meteorol. Soc.*, 143, 607–633, <https://doi.org/10.1002/qj.2982>, 2017.

655 Bergamaschi, P., Krol, M., Meirink, J. F., Dentener, F., Segers, A., van Aardenne, J., Monni, S., Vermeulen, A. T., Schmidt, M., Ramonet, M., Yver, C., Meinhardt, F., Nisbet, E. G., Fisher, R. E., O'Doherty, S., and Dlugokencky, E. J.: Inverse Modeling of European CH<sub>4</sub> Emissions 2001–2006, *J. Geophys. Res.*, 115, D22 309, <https://doi.org/10.1029/2010JD014180>, 2010.

Brasseur, G. P., Xie, Y., Petersen, A. K., Bouarar, I., Flemming, J., Gauss, M., Jiang, F., Kouznetsov, R., Kranenburg, R., Mijling, B., Peuch, V.-H., Pommier, M., Segers, A., Sofiev, M., Timmermans, R., van der A, R., Walters, S., Xu, J., and Zhou, G.: Ensemble Forecasts of Air 660 Quality in Eastern China – Part 1: Model Description and Implementation of the MarcoPolo–Panda Prediction System, Version 1, *Geosci. Model Dev.*, 12, 33–67, <https://doi.org/10.5194/gmd-12-33-2019>, 2019.

Brewster, K. A.: Phase-Correcting Data Assimilation and Application to Storm-Scale Numerical Weather Prediction. Part I: Method Description and Simulation Testing, *Mon. Weather Rev.*, 131, 480–492, [https://doi.org/10.1175/1520-0493\(2003\)131<0480:PCDAAA>2.0.CO;2](https://doi.org/10.1175/1520-0493(2003)131<0480:PCDAAA>2.0.CO;2), 2003.

665 Brunner, D., Henne, S., Keller, C. A., Reimann, S., Vollmer, M. K., O'Doherty, S., and Maione, M.: An Extended Kalman-filter for Regional Scale Inverse Emission Estimation, *Atmos. Chem. Phys.*, 12, 3455–3478, <https://doi.org/10.5194/acp-12-3455-2012>, 2012.

Burgers, G., Jan van Leeuwen, P., and Evensen, G.: Analysis Scheme in the Ensemble Kalman Filter, *Mon. Weather Rev.*, 126, 1719–1724, [https://doi.org/10.1175/1520-0493\(1998\)126<1719:ASITEK>2.0.CO;2](https://doi.org/10.1175/1520-0493(1998)126<1719:ASITEK>2.0.CO;2), 1998.

Chen, L. and Walsh, M.: Vast Sandstorms Expose Mongolia's Long-Ignored Ecological Crisis, 2021.

670 Corazza, M., Bergamaschi, P., Vermeulen, A. T., Aalto, T., Haszpra, L., Meinhardt, F., O'Doherty, S., Thompson, R., Moncrieff, J., Popa, E., Steinbacher, M., Jordan, A., Dlugokencky, E., Brühl, C., Krol, M., and Dentener, F.: Inverse Modelling of European N<sub>2</sub>O Emissions: Assimilating Observations from Different Networks, *Atmos. Chem. Phys.*, 11, 2381–2398, <https://doi.org/10.5194/acp-11-2381-2011>, 2011.

Curier, R., Timmermans, R., Calabretta-Jongen, S., Eskes, H., Segers, A., Swart, D., and Schaap, M.: Improving Ozone Forecasts over 675 Europe by Synergistic Use of the LOTOS-EUROS Chemical Transport Model and in-Situ Measurements, *Atmos. Environ.*, 60, 217–226, <https://doi.org/10.1016/j.atmosenv.2012.06.017>, 2012.

Dance, S. L.: Issues in High Resolution Limited Area Data Assimilation for Quantitative Precipitation Forecasting, *Physica D*, 196, 1–27, <https://doi.org/10.1016/j.physd.2004.05.001>, 2004.

Di Tomaso, E., Schutgens, N. A. J., Jorba, O., and Pérez García-Pando, C.: Assimilation of MODIS Dark Target and Deep Blue Observations 680 in the Dust Aerosol Component of NMMB-MONARCH Version 1.0, *Geosci. Model Dev.*, 10, 1107–1129, <https://doi.org/10.5194/gmd-10-1107-2017>, 2017.

Di Tomaso, E., Escribano, J., Basart, S., Ginoux, P., Macchia, F., Barnaba, F., Benincasa, F., Bretonnière, P.-A., Buñuel, A., Castrillo, M., Cuevas, E., Formenti, P., Gonçalves, M., Jorba, O., Klose, M., Mona, L., Montané Pinto, G., Mytilinaios, M., Obiso, V., Olid, M.,

685 Schutgens, N., Votsis, A., Werner, E., and Pérez García-Pando, C.: The MONARCH High-Resolution Reanalysis of Desert Dust Aerosol over Northern Africa, the Middle East and Europe (2007–2016), *Earth Syst. Sci. Data*, 14, 2785–2816, <https://doi.org/10.5194/essd-14-2785-2022>, 2022.

Duncan Fairlie, T., Jacob, D. J., and Park, R. J.: The Impact of Transpacific Transport of Mineral Dust in the United States, *Atmos. Environ.*, 41, 1251–1266, <https://doi.org/10.1016/j.atmosenv.2006.09.048>, 2007.

Escribano, J., Boucher, O., Chevallier, F., and Huneeus, N.: Impact of the Choice of the Satellite Aerosol Optical Depth Product in a Sub-690 Regional Dust Emission Inversion, *Atmos. Chem. Phys.*, 17, 7111–7126, <https://doi.org/10.5194/acp-17-7111-2017>, 2017.

Evensen, G.: Sequential Data Assimilation with a Nonlinear Quasi-Geostrophic Model Using Monte Carlo Methods to Forecast Error Statistics, *J. Geophys. Res.*, 99, 10 143, <https://doi.org/10.1029/94JC00572>, 1994.

Filonchyk, M. and Peterson, M.: Development, Progression, and Impact on Urban Air Quality of the Dust Storm in Asia in March 15–18, 2021, *Urban Clim.*, 41, 101 080, <https://doi.org/10.1016/j.uclim.2021.101080>, 2022.

695 Foroutan, H. and Pleim, J. E.: Improving the Simulation of Convective Dust Storms in Regional-to-Global Models, *J. Adv. Model. Earth Syst.*, 9, 2046–2060, <https://doi.org/10.1002/2017MS000953>, 2017.

Foroutan, H., Young, J., Napelenok, S., Ran, L., Appel, K. W., Gilliam, R. C., and Pleim, J. E.: Development and Evaluation of a Physics-Based Windblown Dust Emission Scheme Implemented in the CMAQ Modeling System, *J. Adv. Model. Earth Syst.*, 9, 585–608, <https://doi.org/10.1002/2016MS000823>, 2017.

700 Gaspari, G. and Cohn, S. E.: Construction of Correlation Functions in Two and Three Dimensions, *Q. J. R. Meteorol. Soc.*, 125, 723–757, <https://doi.org/10.1002/qj.49712555417>, 1999.

Gasperoni, N. A., Wang, X., and Wang, Y.: Using a Cost-Effective Approach to Increase Background Ensemble Member Size within the GSI-Based EnVar System for Improved Radar Analyses and Forecasts of Convective Systems, *Mon. Weather Rev.*, 150, 667–689, <https://doi.org/10.1175/MWR-D-21-0148.1>, 2022.

705 Gasperoni, N. A., Wang, X., and Wang, Y.: Valid Time Shifting for an Experimental RRFS Convection-Allowing EnVar Data Assimilation and Forecast System: Description and Systematic Evaluation in Real Time, *Mon. Weather Rev.*, 151, 1229–1245, <https://doi.org/10.1175/MWR-D-22-0089.1>, 2023.

Ginoux, P., Chin, M., Tegen, I., Prospero, J. M., Holben, B., Dubovik, O., and Lin, S.-J.: Sources and Distributions of Dust Aerosols Simulated with the GOCART Model, *J. Geophys. Res.*, 106, 20 255–20 273, <https://doi.org/10.1029/2000JD000053>, 2001.

710 Ginoux, P., Prospero, J. M., Gill, T. E., Hsu, N. C., and Zhao, M.: Global-Scale Attribution of Anthropogenic and Natural Dust Sources and Their Emission Rates Based on MODIS Deep Blue Aerosol Products, *Rev. Geophys.*, 50, <https://doi.org/10.1029/2012RG000388>, 2012.

Gong, S. L. and Zhang, X. Y.: CUACE/Dust – an Integrated System of Observation and Modeling Systems for Operational Dust Forecasting in Asia, *Atmos. Chem. Phys.*, 8, 2333–2340, <https://doi.org/10.5194/acp-8-2333-2008>, 2008.

Goudie, A. S.: Desert Dust and Human Health Disorders, *Environ. Int.*, 63, 101–113, <https://doi.org/10.1016/j.envint.2013.10.011>, 2014.

715 Gross, J. E., Carlos, W. G., Dela Cruz, C. S., Harber, P., and Jamil, S.: Sand and Dust Storms: Acute Exposure and Threats to Respiratory Health, *AM J RESP CRIT CARE*, 198, P13–P14, <https://doi.org/10.1164/rccm.1987P13>, 2018.

Gui, K., Yao, W., Che, H., An, L., Zheng, Y., Li, L., Zhao, H., Zhang, L., Zhong, J., Wang, Y., and Zhang, X.: Record-Breaking Dust Loading during Two Mega Dust Storm Events over Northern China in March 2021: Aerosol Optical and Radiative Properties and Meteorological Drivers, *Atmos. Chem. Phys.*, 22, 7905–7932, <https://doi.org/10.5194/acp-22-7905-2022>, 2022.

720 Hamill, T. M.: Ensemble-Based Atmospheric Data Assimilation, in: *Predictability of Weather and Climate*, edited by Palmer, T. and Hagedorn, R., pp. 124–156, Cambridge University Press, 1 edn., <https://doi.org/10.1017/CBO9780511617652.007>, 2006.

Houtekamer, P. L. and Zhang, F.: Review of the Ensemble Kalman Filter for Atmospheric Data Assimilation, *Mon. Weather Rev.*, 144, 4489–4532, <https://doi.org/10.1175/MWR-D-15-0440.1>, 2016.

Houtekamer, P. L., Mitchell, H. L., Pellerin, G., Buehner, M., Charron, M., Spacek, L., and Hansen, B.: Atmospheric Data Assimilation with an Ensemble Kalman Filter: Results with Real Observations, *Mon. Weather Rev.*, 133, 604–620, <https://doi.org/10.1175/MWR-2864.1>, 2005.

Houtekamer, P. L., Deng, X., Mitchell, H. L., Baek, S.-J., and Gagnon, N.: Higher Resolution in an Operational Ensemble Kalman Filter, *Mon. Weather Rev.*, 142, 1143–1162, <https://doi.org/10.1175/MWR-D-13-00138.1>, 2014.

Hu, Z., Huang, J., Zhao, C., Bi, J., Jin, Q., Qian, Y., Leung, L. R., Feng, T., Chen, S., and Ma, J.: Modeling the Contributions of Northern Hemisphere Dust Sources to Dust Outflow from East Asia, *Atmos. Environ.*, 202, 234–243, <https://doi.org/10.1016/j.atmosenv.2019.01.022>, 2019.

Huang, B. and Wang, X.: On the Use of Cost-Effective Valid-Time-Shifting (VTS) Method to Increase Ensemble Size in the GFS Hybrid 4DEnVar System, *Mon. Weather Rev.*, 146, 2973–2998, <https://doi.org/10.1175/MWR-D-18-0009.1>, 2018.

Jin, G.: The Most Severe Sandstorm in a Decade, 2021.

Jin, J.: Ground-Based Air Quality Measurements during the 2021 Spring Super Dust Storms, <https://doi.org/10.5281/zenodo.6459866>, 2022.

Jin, J., Lin, H. X., Heemink, A., and Segers, A.: Spatially Varying Parameter Estimation for Dust Emissions Using Reduced-Tangent-Linearization 4DVar, *Atmos. Environ.*, 187, 358–373, <https://doi.org/10.1016/j.atmosenv.2018.05.060>, 2018.

Jin, J., Lin, H. X., Segers, A., Xie, Y., and Heemink, A.: Machine Learning for Observation Bias Correction with Application to Dust Storm Data Assimilation, *Atmos. Chem. Phys.*, 19, 10 009–10 026, <https://doi.org/10.5194/acp-19-10009-2019>, 2019a.

Jin, J., Segers, A., Heemink, A., Yoshida, M., Han, W., and Lin, H.-X.: Dust Emission Inversion Using Himawari-8 AODs Over East Asia: An Extreme Dust Event in May 2017, *J. Adv. Model. Earth Syst.*, 11, 446–467, <https://doi.org/10.1029/2018MS001491>, 2019b.

Jin, J., Segers, A., Liao, H., Heemink, A., Kranenburg, R., and Lin, H. X.: Source Backtracking for Dust Storm Emission Inversion Using an Adjoint Method: Case Study of Northeast China, *Atmos. Chem. Phys.*, 20, 15 207–15 225, <https://doi.org/10.5194/acp-20-15207-2020>, 2020.

Jin, J., Segers, A., Lin, H. X., Henzing, B., Wang, X., Heemink, A., and Liao, H.: Position Correction in Dust Storm Forecasting Using LOTOS-EUROS v2.1: Grid-Distorted Data Assimilation v1.0, *Geosci. Model Dev.*, 14, 5607–5622, <https://doi.org/10.5194/gmd-14-5607-2021>, 2021.

Jin, J., Pang, M., Segers, A., Han, W., Fang, L., Li, B., Feng, H., Lin, H. X., and Liao, H.: Inverse Modeling of the 2021 Spring Super Dust Storms in East Asia, *Atmos. Chem. Phys.*, 22, 6393–6410, <https://doi.org/10.5194/acp-22-6393-2022>, 2022.

Kalman, R. E.: A New Approach to Linear Filtering and Prediction Problems, *J. Basic Eng.*, 82, 35–45, <https://doi.org/10.1115/1.3662552>, 1960.

Katzfuss, M., Stroud, J. R., and Wikle, C. K.: Understanding the Ensemble Kalman Filter, *The American Statistician*, 70, 350–357, <https://doi.org/10.1080/00031305.2016.1141709>, 2016.

Kok, J. F., Mahowald, N. M., Fratini, G., Gillies, J. A., Ishizuka, M., Leys, J. F., Mikami, M., Park, M.-S., Park, S.-U., Van Pelt, R. S., and Zobeck, T. M.: An Improved Dust Emission Model – Part 1: Model Description and Comparison against Measurements, *Atmos. Chem. Phys.*, 14, 13 023–13 041, <https://doi.org/10.5194/acp-14-13023-2014>, 2014.

Kranenburg, R., Segers, A. J., Hendriks, C., and Schaap, M.: Source Apportionment Using LOTOS-EUROS: Module Description and Evaluation, *Geosci. Model Dev.*, 6, 721–733, <https://doi.org/10.5194/gmd-6-721-2013>, 2013.

Law, K. J. H. and Stuart, A. M.: Evaluating Data Assimilation Algorithms, *Mon. Weather Rev.*, 140, 3757–3782, 760 <https://doi.org/10.1175/MWR-D-11-00257.1>, 2012.

Leeuwen, P. J., Künsch, H. R., Nerger, L., Potthast, R., and Reich, S.: Particle Filters for High-dimensional Geoscience Applications: A Review, *Q. J. R. Meteorol. Soc.*, 145, 2335–2365, <https://doi.org/10.1002/qj.3551>, 2019.

Lei, J., Bickel, P., and Snyder, C.: Comparison of Ensemble Kalman Filters under Non-Gaussianity, *Mon. Weather Rev.*, 138, 1293–1306, 765 <https://doi.org/10.1175/2009MWR3133.1>, 2010.

Liu, Y., Xing, J., Wang, S., Fu, X., and Zheng, H.: Source-Specific Speciation Profiles of PM<sub>2.5</sub> for Heavy Metals and Their Anthropogenic Emissions in China, *Environ. Pollut.*, 239, 544–553, <https://doi.org/10.1016/j.envpol.2018.04.047>, 2018.

Lopez-Restrepo, S., Yarce, A., Pinel, N., Quintero, O., Segers, A., and Heemink, A.: Forecasting PM<sub>10</sub> and PM<sub>2.5</sub> in the Aburrá Valley (Medellín, Colombia) via EnKF Based Data Assimilation, *Atmos. Environ.*, 232, 117507, <https://doi.org/10.1016/j.atmosenv.2020.117507>, 2020.

Lu, H., Xu, Q., Yao, M., and Gao, S.: Time-Expanded Sampling for Ensemble-Based Filters: Assimilation Experiments with Real Radar 770 Observations, *Adv. Atmos. Sci.*, 28, 743–757, <https://doi.org/10.1007/s00376-010-0021-4>, 2011.

Mallet, V. and Sportisse, B.: Uncertainty in a Chemistry-Transport Model Due to Physical Parameterizations and Numerical Approximations: An Ensemble Approach Applied to Ozone Modeling, *J. Geophys. Res.*, 111, <https://doi.org/10.1029/2005JD006149>, 2006.

Manders, A. M. M., Builtjes, P. J. H., Curier, L., Denier van der Gon, H. A. C., Hendriks, C., Jonkers, S., Kranenburg, R., Kuenen, J. J. P., 775 Segers, A. J., Timmermans, R. M. A., Visschedijk, A. J. H., Wichink Kruit, R. J., van Pul, W. A. J., Sauter, F. J., van der Swaluw, E., Swart, D. P. J., Douros, J., Eskes, H., van Meijgaard, E., van Ulft, B., van Velthoven, P., Banzhaf, S., Mues, A. C., Stern, R., Fu, G., Lu, S., Heemink, A., van Velzen, N., and Schaap, M.: Curriculum Vitae of the LOTOS-EUROS (v2.0) Chemistry Transport Model, *Geosci. Model Dev.*, 10, 4145–4173, <https://doi.org/10.5194/gmd-10-4145-2017>, 2017.

Marticorena, B. and Bergametti, G.: Modeling the Atmospheric Dust Cycle: 1. Design of a Soil-Derived Dust Emission Scheme, *J. Geophys. Res.*, 100, 16 415, <https://doi.org/10.1029/95JD00690>, 1995.

Mona, L., Papagiannopoulos, N., Basart, S., Baldasano, J., Binietoglou, I., Cornacchia, C., and Pappalardo, G.: EARLINET Dust Observations vs. BSC-DREAM8b Modeled Profiles: 12-Year-Long Systematic Comparison at Potenza, Italy, *Atmos. Chem. Phys.*, 14, 8781–8793, 780 <https://doi.org/10.5194/acp-14-8781-2014>, 2014.

Muhammad Akhlaq, Sheltami, T. R., and Mouftah, H. T.: A Review of Techniques and Technologies for Sand and Dust Storm Detection, *Rev. Environ. Sci. Bio.*, 11, 305–322, <https://doi.org/10.1007/s11157-012-9282-y>, 2012.

Nehrkorn, T., Woods, B. K., Hoffman, R. N., and Auligné, T.: Correcting for Position Errors in Variational Data Assimilation, *Mon. Weather Rev.*, 143, 1368–1381, <https://doi.org/10.1175/MWR-D-14-00127.1>, 2015.

Pang, M.: Source Code of PyFilter, Zenodo, <https://doi.org/10.5281/zenodo.7611976>, last access: May. 2024.

Pang, M., Jin, J., Segers, A., Jiang, H., Fang, L., Lin, H. X., and Liao, H.: Dust Storm Forecasting through Coupling LOTOS-EUROS with 785 Localized Ensemble Kalman Filter, *Atmos. Environ.*, 306, 119 831, <https://doi.org/10.1016/j.atmosenv.2023.119831>, 2023.

Park, S.-Y., Dash, U. K., Yu, J., Yumimoto, K., Uno, I., and Song, C. H.: Implementation of an Ensemble Kalman Filter in the Community Multiscale Air Quality Model (CMAQ Model v5.1) for Data Assimilation of Ground-Level PM<sub>2.5</sub>, *Geosci. Model Dev.*, 15, 2773–2790, 790 <https://doi.org/10.5194/gmd-15-2773-2022>, 2022.

Pérez, C., Nickovic, S., Baldasano, J. M., Sicard, M., Rocadenbosch, F., and Cachorro, V. E.: A Long Saharan Dust Event over the Western Mediterranean: Lidar, Sun Photometer Observations, and Regional Dust Modeling, *J. Geophys. Res.*, 111, D15 214, 795 <https://doi.org/10.1029/2005JD006579>, 2006.

Pommier, M., Fagerli, H., Schulz, M., Valdebenito, A., Kranenburg, R., and Schaap, M.: Prediction of Source Contributions to Urban Background PM<sub>10</sub> Concentrations in European Cities: A Case Study for an Episode in December 2016 Using EMEP/MSC-W Rv4.15 and LOTOS-EUROS v2.0 – Part 1: The Country Contributions, *Geosci. Model Dev.*, 13, 1787–1807, <https://doi.org/10.5194/gmd-13-1787-2020>, 2020.

800 Rabier, F. and Liu, Z.: Variational Data Assimilation: Theory and Overview, in: Proc. ECMWF Seminar on Recent Developments in Data Assimilation for Atmosphere and Ocean, Reading, UK, September 8–12, pp. 29–43, 2003.

Ravela, S., Emanuel, K., and McLaughlin, D.: Data Assimilation by Field Alignment, *Physica D*, 230, 127–145, <https://doi.org/10.1016/j.physd.2006.09.035>, 2007.

Reichle, R. H., McLaughlin, D. B., and Entekhabi, D.: Hydrologic Data Assimilation with the Ensemble Kalman Filter, *Mon. Weather Rev.*, 130, 103–114, [https://doi.org/10.1175/1520-0493\(2002\)130<0103:HDAWTE>2.0.CO;2](https://doi.org/10.1175/1520-0493(2002)130<0103:HDAWTE>2.0.CO;2), 2002.

805 Shao, Y.: Simplification of a Dust Emission Scheme and Comparison with Data, *J. Geophys. Res.*, 109, D10202, <https://doi.org/10.1029/2003JD004372>, 2004.

Shao, Y., Raupach, M., and Leys, J.: A Model for Predicting Aeolian Sand Drift and Dust Entrainment on Scales from Paddock to Region, *Soil Res.*, 34, 309, <https://doi.org/10.1071/SR9960309>, 1996.

810 She, L., Xue, Y., Guang, J., Che, Y., Fan, C., Li, Y., and Xie, Y.: Towards a Comprehensive View of Dust Events from Multiple Satellite and Ground Measurements: Exemplified by the May 2017 East Asian Dust Storm, *Nat. Hazards Earth Syst. Sci.*, 18, 3187–3201, <https://doi.org/10.5194/nhess-18-3187-2018>, 2018.

Skoulidou, I., Koukouli, M.-E., Manders, A., Segers, A., Karagkiozidis, D., Gratsea, M., Balis, D., Bais, A., Gerasopoulos, E., Stavrakou, T., van Geffen, J., Eskes, H., and Richter, A.: Evaluation of the LOTOS-EUROS NO<sub>2</sub> Simulations Using Ground-Based Measurements and 815 S5P/TROPOMI Observations over Greece, *Atmos. Chem. Phys.*, 21, 5269–5288, <https://doi.org/10.5194/acp-21-5269-2021>, 2021.

Song, L., Bi, X., Zhang, Z., Li, L., Dai, Q., Zhang, W., Li, H., Wang, X., Liang, D., and Feng, Y.: Impact of Sand and Dust Storms on the Atmospheric Environment and Its Source in Tianjin-China, *Sci. Total Environ.*, 825, 153 980, <https://doi.org/10.1016/j.scitotenv.2022.153980>, 2022.

Tang, W., Dai, T., Cheng, Y., Wang, S., and Liu, Y.: A Study of a Severe Spring Dust Event in 2021 over East Asia with WRF-Chem and 820 Multiple Platforms of Observations, *Remote Sens.*, 14, 3795, <https://doi.org/10.3390/rs14153795>, 2022.

Timmermans, R., Kranenburg, R., Manders, A., Hendriks, C., Segers, A., Dammers, E., Zhang, Q., Wang, L., Liu, Z., Zeng, L., Denier van der Gon, H., and Schaap, M.: Source Apportionment of PM<sub>2.5</sub> across China Using LOTOS-EUROS, *Atmos. Environ.*, 164, 370–386, <https://doi.org/10.1016/j.atmosenv.2017.06.003>, 2017.

TNO: Source Code and User Guidance of LOTOS-EUROS, TNO, last access: May 2024.

825 Wang, X.: Historical data on air quality in china, <https://quotsoft.net/air/>, last access: May. 2024.

Wu, X., Vu, T. V., Shi, Z., Harrison, R. M., Liu, D., and Cen, K.: Characterization and Source Apportionment of Carbonaceous PM<sub>2.5</sub> Particles in China - A Review, *Atmos. Environ.*, 189, 187–212, <https://doi.org/10.1016/j.atmosenv.2018.06.025>, 2018.

Xu, Q., Wei, L., Lu, H., Qiu, C., and Zhao, Q.: Time-Expanded Sampling for Ensemble-Based Filters: Assimilation Experiments with a Shallow-Water Equation Model, *J. Geophys. Res.*, 113, <https://doi.org/10.1029/2007JD008624>, 2008.

830 Yarce Botero, A., Lopez-Restrepo, S., Pinel Peláez, N., Quintero, O. L., Segers, A., and Heemink, A. W.: Estimating NO<sub>x</sub> LOTOS-EUROS CTM Emission Parameters over the Northwest of South America through 4DEnVar TROPOMI NO<sub>2</sub> Assimilation, *Atmosphere-Basel*, 12, 1633, <https://doi.org/10.3390/atmos12121633>, 2021.

Yumimoto, K. and Takemura, T.: Long-Term Inverse Modeling of Asian Dust: Interannual Variations of Its Emission, Transport, Deposition, and Radiative Forcing, *J. Geophys. Res. Atmos.*, 120, 1582–1607, <https://doi.org/10.1002/2014JD022390>, 2015.

835 Zender, C. S., Bian, H., and Newman, D.: Mineral Dust Entrainment and Deposition (DEAD) Model: Description and 1990s Dust Climatology, *J. Geophys. Res.*, 108, <https://doi.org/10.1029/2002JD002775>, 2003.

Zhang, R., Arimoto, R., An, J., Yabuki, S., and Sun, J.: Ground Observations of a Strong Dust Storm in Beijing in March 2002, *J. Geophys. Res.*, 110, <https://doi.org/10.1029/2004JD004589>, 2005.

840 Zhang, X., Sharratt, B., Liu, L., Wang, Z., Pan, X., Lei, J., Wu, S., Huang, S., Guo, Y., Li, J., Tang, X., Yang, T., Tian, Y., Chen, X., Hao, J., Zheng, H., Yang, Y., and Lyu, Y.: East Asian Dust Storm in May 2017: Observations, Modelling, and Its Influence on the Asia-Pacific Region, *Atmos. Chem. Phys.*, 18, 8353–8371, <https://doi.org/10.5194/acp-18-8353-2018>, 2018.

Zhao, Q., Xu, Q., Jin, Y., McLay, J., and Reynolds, C.: Time-Expanded Sampling for Ensemble-Based Data Assimilation Applied to Conventional and Satellite Observations, *Weather Forecasting*, 30, 855–872, <https://doi.org/10.1175/WAF-D-14-00108.1>, 2015.